Air–Sea Enthalpy and Momentum Exchange at Major Hurricane Wind Speeds Observed during CBLAST

MICHAEL M. BELL

Department of Meteorology, Naval Postgraduate School, Monterey, California, and National Center for Atmospheric Research, Boulder, Colorado*

MICHAEL T. MONTGOMERY

Department of Meteorology, Naval Postgraduate School, Monterey, California, and NOAA/Hurricane Research Division, Miami, Florida

KERRY A. EMANUEL

Department of Earth, Atmospheric and Planetary Sciences, Massachusetts Institute of Technology, Cambridge, Massachusetts

(Manuscript received 17 October 2011, in final form 4 April 2012)

ABSTRACT

Quantifying air–sea exchanges of enthalpy and momentum is important for understanding and skillfully predicting tropical cyclone intensity, but the magnitude of the corresponding wind speed–dependent bulk exchange coefficients is largely unknown at major hurricane wind speeds greater than 50 m s^{-1}. Since direct turbulent flux measurements in these conditions are extremely difficult, the momentum and enthalpy fluxes were deduced via absolute angular momentum and total energy budgets. An error analysis of the methodology was performed to quantify and mitigate potentially significant uncertainties resulting from unresolved budget terms and observational errors. An analysis of six missions from the 2003 Coupled Boundary Layers Air–Sea Transfer (CBLAST) field program in major hurricanes Fabian and Isabel was conducted using a new variational technique. The analysis indicates a near-surface mean drag coefficient C_D of 2.4×10^{-3} with a 46% standard deviation and a mean enthalpy coefficient C_K of 1.0×10^{-3} with a 40% standard deviation for wind speeds between 52 and 72 m s^{-1}. These are the first known estimates of C_K and the ratio of enthalpy to drag coefficient C_K/C_D in major hurricanes. The results suggest that there is no significant change in the magnitude of the bulk exchange coefficients estimated at minimal hurricane wind speeds, and that the ratio C_K/C_D does not significantly increase for wind speeds greater than 50 m s^{-1}.

1. Introduction

Heat, moisture, and momentum exchanges at the air–sea interface are primary processes in tropical cyclone (TC) intensification and maintenance (Malkus and Riehl 1960; Emanuel 1986, 1995). Wind speed–dependent bulk aerodynamic formulas often are used to represent the turbulent fluxes associated with air–sea interactions, relying on drag C_D, moisture C_E, and enthalpy C_K exchange coefficients. However, as Ooyama (1969) stated, ''Unfortunately, there is little information on C_E under hurricane conditions, other than the semispeculative guess that the exchange coefficients of latent heat, sensible heat, and momentum are probably of the same magnitude.'' Nearly 40 yr after that pioneering study, enthalpy and momentum exchange coefficients are still largely unknown at major hurricane wind speeds (>50 m s^{-1}, equivalent to category 3 and higher on the

* The National Center for Atmospheric Research is sponsored by the National Science Foundation.

Corresponding author address: Michael M. Bell, University of Hawaii at Manoa, Department of Meteorology, 2525 Correa Road, Honolulu, HI 96822.
E-mail: mmbell@hawaii.edu

DOI: 10.1175/JAS-D-11-0276.1

Saffir–Simpson scale). Since the ocean surface characteristics change significantly with increasing wind speed (Black et al. 1986), a simple extrapolation of the coefficient magnitudes derived at low wind speeds to 50 m s^{-1} and beyond is not necessarily justified. The current research aims to improve our understanding of air–sea interaction in major hurricanes, given the high impact that their damaging winds and storm surge can have on coastal populations, global economics, maritime activities, and naval operations.

Emanuel (1986) derived an expression for the potential intensity (hereafter E-PI) of a TC that depends on local environmental parameters and is proportional to the ratio of the bulk enthalpy and momentum exchange coefficients C_K/C_D. Montgomery et al. (2006) and Bell and Montgomery (2008, hereafter BM08) showed that a 30 m s^{-1} range of E-PI estimates for category 5 Hurricane Isabel (2003) could be obtained by varying the magnitude of this ratio from 0.5 to 1.5. More refined estimates of the bulk exchange coefficients would clearly help narrow the uncertainty in E-PI predictions. The importance of understanding of air–sea exchange at high wind speeds is not limited to the theoretical domain, however. E-PI estimates are used in statistical TC intensity forecasts (Emanuel et al. 2004), and numerically simulated intensity has shown sensitivity to prescribed surface exchange coefficients in a variety of simplified model frameworks (Ooyama 1969; Rosenthal 1971; Rotunno and Emanuel 1987; Emanuel 1995). Three-dimensional, full physics models have also shown sensitivity to the parameterization of surface fluxes in hurricane intensity forecasts (Braun and Tao 2000; Bao et al. 2002; Davis et al. 2008). It must be noted that parameterizing the complexity of the air–sea interaction at these wind speeds with 10-m bulk exchange coefficients is likely an oversimplification, but accurate estimates are still important given the established practical reliance on these coefficients. Improvements in numerical weather models' representation of air–sea interaction in major tropical cyclones would likely contribute to improved intensity forecasts issued by the Joint Typhoon Warning Center and the National Hurricane Center (NHC) (Rappaport et al. 2009).

Surface fluxes at major hurricane wind speeds are very difficult to measure in the tropical cyclone boundary layer (TCBL). Given that the spatial and temporal occurrence of these wind speeds is very small compared to the ocean basin size and seasonal time scales in which hurricanes occur, the probability of a fixed sensor encountering them is very low. Instrumented ships prudently avoid these conditions in general, and operational ocean sensors (such as buoys) are not designed to withstand the extreme conditions found in the open ocean at the base of a major hurricane eyewall. Therefore, laboratory experiments and observations from research aircraft deployed in tropical cyclones are currently the most viable choices for obtaining information about surface fluxes at high wind speeds. However, low-altitude flying in the turbulent boundary layer at the base of an eyewall is also very hazardous, which requires that remote sensing or expendables (i.e., dropwindsondes) be used to obtain measurements in this region.

Global positioning system dropwindsonde (hereafter simply dropsonde) profiles have been used to estimate flux profiles and C_D at the highest wind speeds yet (Powell et al. 2003; Vickery et al. 2009). Powell et al. (2003) provided the first indications of a slight decrease in C_D from maximum values around 2.5×10^{-3} at 30–40 m s^{-1}. Dropsonde profiles analyzed by Vickery et al. (2009) indicated a continued slight decrease in C_D at wind speeds up to 60 m s^{-1}. Additional evidence that C_D does not increase above 35 m s^{-1} was reported by Donelan et al. (2004) using laboratory tank measurements. The eddy correlation method was used for wind speeds up to 26 m s^{-1}, and a momentum budget retrieval was used for wind speeds from 20–50 m s^{-1}. These tank measurements showed a ''saturation'' of C_D around hurricane-force wind speed (33 m s^{-1}) and suggested a limiting aerodynamic roughness of the surface waves above these speeds. Indirect retrievals of C_D in hurricanes that are consistent with the above studies have also been conducted using ocean measurements (Shay and Jacob 2006; Jarosz et al. 2007).

The uncertainty in the magnitude of C_D and C_K in the TCBL was one of the issues investigated as part of the Coupled Boundary Layers Air–Sea Transfer (CBLAST) field campaign (Black et al. 2007). Because of the safety hazards mentioned previously, instrumented P-3 aircraft were only flown in the clear air boundary layer between rainbands, but fortunately favorable conditions for turbulence observations were achieved in two major hurricanes, Fabian and Isabel (2003). French et al. (2007) and Drennan et al. (2007) reported the first open-ocean eddy correlation measurements in the TCBL at strong tropical storm force wind speeds (20–30 m s^{-1}). Estimates of C_D and C_E from these studies indicated no discernible dependence on wind speed in the range measured. Although the French et al. (2007) results slightly differ from those reported by Powell et al. (2003) and Donelan et al. (2004), general agreement exists that an extrapolation of an increasing C_D from low wind speed formulas (e.g., Large and Pond 1981) is not justified. Recent research suggest that C_K is nearly independent of wind speed from 20 to 30 m s^{-1} using the CBLAST measurements

(Zhang et al. 2008) and from 13 to 40 m s^{-1} using laboratory measurements (Haus et al. 2010; Jeong et al. 2012). There have been no previous estimates of the magnitude of C_K at major hurricane wind speeds to the authors' knowledge.

Emanuel (2003) developed a similarity theory for gradient wind-based exchange coefficients at very high wind speeds and suggested, based on an asymptotic analysis, that both exchange coefficients should approach constant values in the limit of high wind speed. He also presented a mechanistic argument that suggests that the ratio of enthalpy to momentum coefficients should decrease with increasing ocean temperature. But neither of these approaches predicts specific values of the exchange coefficients. The scaling theory of Emanuel (2003) is based on the gradient wind and neglects the explicit role of the (unbalanced) boundary layer dynamics and their contribution to the total wind speed. The total wind speed is the intensity measure of most interest to hurricane forecasters.

An indirect approach to retrieving momentum exchange using an absolute angular momentum budget was originally proposed over 50 yr ago (Palmén and Riehl 1957). In their formulation, the surface stress is obtained by measured transports of absolute angular momentum in an axisymmetric cylindrical coordinate system. If the flux of angular momentum is known at the top and sides of a prescribed control volume, the flux at the air–sea interface can be obtained via residual, assuming that the system is in a steady condition. Additional studies used angular momentum budgets to deduce C_D with improved datasets (Miller 1962, 1964; Hawkins and Rubsam 1968; Hawkins and Imbembo 1976). The quality and density of hurricane observations have improved significantly since that time, as well as the analysis techniques used to composite the data. The central focus of our research was the application of a similar methodology to retrieve surface fluxes in major hurricanes using recent observations. In this study, we utilize budgets of absolute angular momentum and total energy to retrieve C_D and C_K in major hurricanes Fabian and Isabel.

In practical application, some of the momentum and energy budget terms are very difficult to calculate with observational data, and uncertainties must be acknowledged. To gain insight into the relative importance of the various sources of error in the budgets, the sensitivity to errors in unresolved budget terms, sea surface temperature (SST), center location, gridding method, and the size of budget control volumes were examined systematically using numerical model data where the surface fluxes were known. The results of the sensitivity tests were then utilized to determine quantitative estimates of the uncertainty of the magnitude of the retrieved bulk exchange coefficients.

A high-resolution dataset collected in Hurricanes Fabian and Isabel in 2003 as part of the CBLAST experiment (Black et al. 2007) was used to apply an energy and momentum budget method to real tropical cyclones. Both TCs achieved category 4 intensity, and the data collected represent a significant advance in the quantity and quality of observations in major hurricanes. To deduce momentum and enthalpy fluxes from these observations using the current methodology, the data are gridded in an axisymmetric coordinate system moving with the tropical cyclone. Montgomery et al. (2006) and BM08 used a simple objective analysis scheme (Barnes 1973) to derive a gridded axisymmetric structure for Hurricane Isabel for use with the E-PI calculations. A new variational analysis procedure called Spline Analysis at Mesoscale Utilizing Radar and Aircraft Instrumentation (SAMURAI) was used here to improve the derived axisymmetric structure used in the budget calculations.

A review of the equations used in the budget calculations and summary of the uncertainties are presented in section 2, with more detailed descriptions of the error analysis and SAMURAI technique provided in the appendices for interested readers. The results of the CBLAST data analysis are presented in section 3, followed by the derived air–sea fluxes and bulk exchange coefficients in section 4. The concluding section summarizes the key findings of this study.

2. Methodology

a. Conservation of absolute angular momentum

To determine the bulk momentum exchange coefficient, we utilize the conservation of azimuthally averaged absolute angular momentum in cylindrical coordinates, defined as $\overline{M}(r,z) \equiv r\overline{v} + (1/2)fr^2$, where r denotes the radius from the storm center, v denotes the tangential (swirling) wind velocity, f denotes the Coriolis parameter, and the overbar represents both an azimuthal and temporal average. For the current analysis, we hold f to be a constant in the azimuthally averaged coordinate system. The equation for conservation of $\overline{M}$ in flux form is given by

$$\frac{\partial(\rho M)}{\partial t} + \frac{\partial(\rho ruM)}{r\partial r} + \frac{\partial(\rho wM)}{\partial z} - \frac{\partial(r^2\tau_{r\theta})}{r\partial r} - \frac{r\partial\tau_{z\theta}}{\partial z} = 0, \tag{1}$$

where the overbars have been dropped for clarity. The Reynolds stresses are defined as $\tau_{r\theta} \equiv -\rho\overline{u'v'}$ and $\tau_{z\theta} \equiv -\rho\overline{w'v'}$, where the subscripts represent the wind

directions of the covariances (r is the radial direction, θ is the tangential direction, and z is the vertical direction), primes represent the departures from the azimuthal and time averages, ρ denotes the density, u denotes the radial wind velocity, and w denotes the vertical velocity. Integrating over a control volume from z_1 to z_2 and r_1 to r_2 yields an integrated flux form over a control volume:

$$\int_{r_1}^{r_2} [\tau_{z\theta}]|_{z_1} r^2\, dr = r_1 \int_{z_1}^{z_2} [\rho u M - r\tau_{r\theta}]|_{r_1}\, dz - r_2 \int_{z_1}^{z_2} [\rho u M - r\tau_{r\theta}]|_{r_2}\, dz + \int_{r_1}^{r_2} [\rho w M]|_{z_1} r\, dr - \int_{r_1}^{r_2} [\rho w M - r\tau_{z\theta}]|_{z_2} r\, dr - \int_{z_1}^{z_2}\int_{r_1}^{r_2} \frac{\partial(\rho M)}{\partial t} r\, dr\, dz. \quad (2)$$

From Eq. (2), the radially integrated surface stress may be calculated from measurements on the sides and top of an arbitrary control volume. A schematic of a hypothetical control volume is shown in Fig. 1, which illustrates the approximate locations of z_1, z_2, r_1, and r_2 for an idealized hurricane flow. We assume that the vertical stress at z_1 can be represented by a bulk formula $\tau_{z\theta} \equiv -\overline{\rho w' v'} = \rho C_D |\mathbf{u}_h| v$, where $|\mathbf{u}_h|$ denotes the horizontal wind speed, and neglect the radial variation of C_D over the control volume to yield the drag coefficient in terms of mean quantities, with unresolved terms grouped into a residual labeled **R**:

$$C_D = \left(r_1 \int_{z_1}^{z_2} [\rho u M]|_{r_1}\, dz - r_2 \int_{z_{z1}}^{z_2} [\rho u M]|_{r_2}\, dz + \int_{r_1}^{r_2} [\rho w M]|_{z_1} r\, dr - \int_{r_1}^{r_2} [\rho w M]|_{z_2} r\, dr + \mathbf{R} \right) \Bigg/ \int_{r_1}^{r_2} [\rho |\mathbf{u}_h| v]|_{z_1} r^2\, dr, \quad (3)$$

where the unresolved residual is

$$\mathbf{R} = -r_1 \int_{z_1}^{z_2} [r\tau_{r\theta}]|_{r_1}\, dz + r_2 \int_{z_1}^{z_2} [r\tau_{r\theta}]|_{r_2}\, dz + \int_{r_1}^{r_2} [r\tau_{z\theta}]|_{z_2} r\, dr - \int_{z_1}^{z_2}\int_{r_1}^{r_2} \frac{\partial(\rho M)}{\partial t} r\, dr\, dz. \quad (4)$$

Alternatively, one can obtain the average surface stress in the control volume by dividing Eq. (2) by $\int_{r_1}^{r_2} r^2\, dr$, or obtain the average friction velocity u^* by dividing Eq. (2) by $-\int_{r_1}^{r_2} \rho r^2\, dr$ and taking the square root. Note that z_1 does not necessarily have to be at 10-m altitude but could be anywhere in the surface layer assuming the fluxes are nearly constant in that layer. If z_1 is higher than 10 m, then the denominator in Eq. (3) must be calculated using the 10-m density and winds to obtain the surface drag coefficient.

b. Conservation of total energy

To determine the bulk moist enthalpy exchange coefficient, we utilize the conservation of total energy, given in flux form in cylindrical coordinates by

$$\frac{\partial(\rho E)}{\partial t} + \frac{\partial(\rho r u E)}{r\partial r} + \frac{\partial(\rho w E)}{\partial z} = \frac{\partial p}{\partial t} + \rho\mu\nabla\left(\frac{1}{2}\mathbf{u}^2\right) + k\nabla^2 T + Q_R, \quad (5)$$

where the total energy $E(r, \theta, z, t) \equiv c_p T + Lq + (1/2)(u^2 + v^2 + w^2) + gz$ is the sum of the internal (sensible and latent heat) energy and mechanical (kinetic and potential) energy of the mean flow. Here c_p denotes the specific heat at constant pressure, T denotes the temperature, L denotes the latent heat of vaporization, q denotes the water vapor mixing ratio, g denotes gravity, μ denotes the molecular viscosity, k denotes the thermal conductivity, and Q_R denotes diabatic heat exchange due to radiative transfer. Equation (5) is a form of Bernoulli's equation (Gill 1982). Because the thermodynamic equation was expressed in terms of the enthalpy instead of the internal energy (e.g., $c_p T = c_v T + p/\rho$), a local time derivative of p appears on the right-hand side that is associated with acoustic waves in the atmosphere. Here, we assume that the local time derivative of p, diffusive component of friction, thermal conductivity, and radiation are small and can be neglected for this application. Reynolds averaging Eq. (5) over azimuth and time and integrating over the control volume yields

$$\int_{r_1}^{r_2}[F_{zk}]|_{z_1} r\,dr = \int_{z_1}^{z_2} r_2[\rho uE + F_{rk} + ue + \overline{u'e} - w\tau_{rz} - v\tau_{r\theta}]|_{r_2}\,dz - \int_{z_1}^{z_2} r_1[\rho uE + F_{rk} + ue + \overline{u'e} - w\tau_{rz} - v\tau_{r\theta}]|_{r_1}\,dz + \int_{r_1}^{r_2}[\rho wE + F_{zk} + we + \overline{w'e} - u\tau_{rz} - v\tau_{z\theta}]|_{z_2} r\,dr - \int_{r_1}^{r_2}[\rho wE + we + \overline{w'e} - u\tau_{rz} - v\tau_{z\theta}]|_{z_1} r\,dr + \int_{z_1}^{z_2}\int_{r_1}^{r_2}\left[\frac{\partial(\rho E + e)}{\partial t}\right] r\,dr\,dz, \quad (6)$$

where all variables represent azimuthal and temporal means, with the bars dropped except over third-order covariance terms for clarity. The turbulent kinetic energy is given by $e \equiv (1/2)\rho(\overline{u'^2} + \overline{v'^2} + \overline{w'^2})$, and the eddy enthalpy fluxes are represented by the F terms, where the subscripts indicate the respective covariances with an oppositely signed convention to the Reynolds stresses. Note that dissipative heating terms do not appear in the total energy balance equation (6) since they represent a conversion between mechanical and heat energy, nor do terms appear involving the conversion of mean kinetic energy to turbulent kinetic energy (e.g., Lindzen 1990, 90–92). However, flux gradients involving the interaction of turbulent momentum fluxes and shearing flow remain. For lack of an established terminology, these terms are referred to as the "shear flux" and represent a transport of energy through the boundaries of the control volume by the interaction of turbulence and the mean flow. For the lower boundary, $F_{\mathrm{SHEAR}} = \int_{r_1}^{r_2}[u\tau_{rz} + v\tau_{z\theta}]$ represents a loss of kinetic energy to the ocean through the interaction of the surface momentum fluxes and mean flow. The shear flux term is not included in the residual since it may be resolved indirectly via the derived surface momentum fluxes.

We assume that the vertical moist enthalpy flux at z_1 can be represented by a bulk formula $F_{zk} = F_{zT} + F_{zq} \equiv \rho c_p \overline{w'T'} + \rho L\overline{w'q'} = C_K \rho |\mathbf{u}_h|(k^* - k)$, where k^* is the saturation moist enthalpy at the sea surface ($k^* = c_p T_{\mathrm{SST}} + Lq^*$) and q^* is the saturation mixing ratio at the surface. Neglecting the radial variation of C_K over the control volume yields the bulk enthalpy exchange coefficient:

$$C_K = \left(\int_{z_1}^{z_2} r_2[\rho uE]|_{r_2}\,dz - \int_{z_1}^{z_2} r_1[\rho uE]|_{r_1}\,dz + \int_{r_1}^{r_2}[\rho wE]|_{z_2} r\,dr - \int_{r_1}^{r_2}[\rho wE]|_{z_1} r\,dr + F_{\mathrm{SHEAR}} + \mathbf{R}\right) \Bigg/ \int_{r_1}^{r_2}[\rho|\mathbf{u}_h|(k^* - k)]|_{z_1} r\,dr. \quad (7)$$

The unresolved residual is

$$\mathbf{R} = \int_{z_1}^{z_2} r_2[F_{rk} + ue + \overline{u'e} - w\tau_{rz} - v\tau_{r\theta}]|_{r_2}\,dz - \int_{z_1}^{z_2} r_1[F_{rk} + ue + \overline{u'e} - w\tau_{rz} - v\tau_{r\theta}]|_{r_1}\,dz + \int_{r_1}^{r_2}[F_{zk} + we + \overline{w'e} - u\tau_{rz} - v\tau_{z\theta}]|_{z_2} r\,dr - \int_{r_1}^{r_2}[we + \overline{w'e}]|_{z_1} r\,dr + \int_{z_1}^{z_2}\int_{r_1}^{r_2}\left[\frac{\partial(\rho E + e)}{\partial t}\right] r\,dr\,dz. \quad (8)$$

Alternatively, one can obtain the average enthalpy flux by dividing Eq. (6) by the radially integrated radius similarly to the average momentum flux. Likewise, if z_1 is higher than 10 m, then the denominator in Eq. (7) must be calculated using the 10-m density, wind, and enthalpy to obtain the surface enthalpy exchange coefficient.

c. Error analysis

Accuracy in the retrieval of the bulk exchange coefficients requires (i) minimal errors in the specification of the axisymmetric kinematic fields, (ii) strict adherence to mass continuity, and (iii) a small magnitude of the unresolved residual terms. Accurate retrieval of C_K

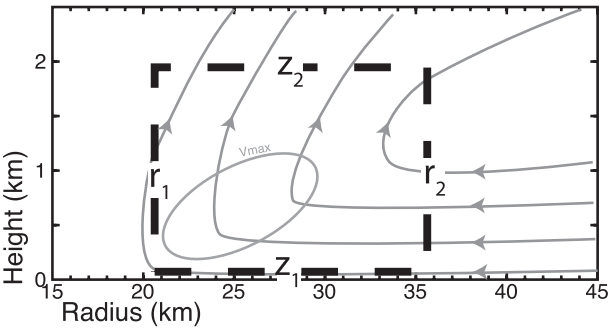

FIG. 1. Schematic illustrating hypothetical control volume (black dashed line) used for the budget methodology. A simplified secondary circulation (gray streamlines) and a contour surrounding the region of maximum wind (gray oval labeled "Vmax") are shown to indicate that the control volume encompasses the eyewall region.

also requires (iv) minimal errors in the axisymmetric thermodynamic fields and (v) accurate measurements of the SST. To test the accuracy of the methodology, comprehensive error analyses were undertaken using idealized numerical simulations. A summary of the errors identified by the sensitivity tests is presented here, and described in more detail for interested readers in appendix A. Table 1 shows the magnitude of potential errors that could affect the solution, steps that were taken to mitigate the error, and the estimated uncertainties remaining after mitigation. If left unconstrained, the unmitigated errors listed can easily overwhelm the magnitudes of the retrieved exchange coefficients, but they are small enough after mitigation to allow meaningful interpretation of the results. The largest source of potential error was estimated to be numerical inaccuracies in the satisfaction of the mass continuity equation. Strict adherence to mass continuity was enforced by using a transverse streamfunction as a control variable in the SAMURAI technique, thereby eliminating this source of error from the solution. The second largest source of error results from the neglect of the unresolved residual terms in the budget. The volume-integrated tendency term and vertical eddy fluxes at the top of the control volume were identified as the largest of these unresolved terms. The error from neglecting these terms manifests primarily as sensitivity to the size and shape of the control volume. An optimal set of control volume sizes was identified to minimize the error, and the remaining uncertainty is estimated at ±50%.

The shear flux term is about 40%–60% of the magnitude of the surface fluxes, which results in a significant low bias if neglected. However, the low bias can be corrected by estimating the shear flux using the mean wind multiplied by the surface stress derived from the momentum budget. The bias correction is exact where the mean winds and C_D are known exactly, but errors in the mean winds and surface stress using real data add some uncertainty. Sensitivity tests indicate that a ±50% error in C_D translates to a ±20% error in the magnitude of C_K from the shear flux term. To avoid adding too much noise to the C_K estimates, a mean C_D derived from all six missions was used in this study to estimate the surface stress used in evaluating the shear flux for C_K. We therefore estimate a C_K uncertainty of ±20% due to the bias correction.

The sensitivity tests also identified analysis errors, SST errors, and circulation center errors as areas where mitigation was required to ensure the best possible results from the observational dataset. Analysis errors were minimized by using a variational approach designed specifically for this study that is described in the next section. SST errors were minimized by using airborne expendable bathythermograph (AXBT) data in combination with satellite-derived temperatures as described in section 3b. The use of high-resolution radar-derived circulation centers minimizes the error in the cylindrical coordinate transform as described in section 3c. The remaining uncertainties for each of the error sources after mitigation are estimated to be on the order of ±20%. Fortunately, these errors are independent and random, and there is no reason to expect that they would be cumulative.

TABLE 1. Summary of estimated errors in the budget retrieval. Error percentages are valid for C_K values of about 2.4×10^{-3} and C_K values of about 1×10^{-3}.

Error source	Unmitigated error	Mitigation	Estimated error
Mass continuity residual	>500%	Use streamfunction for analysis	0%
Unresolved budget residual terms	±200%	Constrain control volume size	±50%
Shear flux term	−60%	Estimate term using derived CD	±20%
SST errors	~20% per 1°C error	Use AXBT data when available	±20%
Center errors	±25% per 1 km error for unaveraged analysis	Use high-resolution radar circulation centers and averaging	±20%
Analysis errors	Large with hand or objective analysis	SAMURAI	±20%

d. SAMURAI

Atmospheric data must be available at regularly spaced intervals to numerically integrate the kinematic and thermodynamic integrals in the budget calculations. For early TC momentum and energy budget studies such as that of Palmén and Riehl (1957), data gridding was done by a manual map analysis that was then interpolated to regular intervals. Manual analysis was largely superseded by the development of objective analysis techniques that created a gridded data field by weighting the observations by their distance from a particular grid point, such as the Barnes (1973) technique used in BM08. Modern data assimilation techniques have continued to improve the analysis of data using more sophisticated variational and probabilistic techniques. For the current study, a two-dimensional variational analysis technique called SAMURAI was developed based primarily on the work of Ooyama (1987, 2002) and Gao et al. (2004). The SAMURAI technique yields a maximum likelihood estimate of the atmospheric state for a given set of observations and error estimates by minimizing a variational cost function. The technique has several advantages over the Barnes (1973) technique used in BM08, including (i) observational error specifications for different instrumentation, (ii) use of more complex observations such as remote sensing data, (iii) the addition of balance constraints such as mass continuity, and (iv) a priori background estimates of the atmospheric state when available.

A distinguishing characteristic of the SAMURAI technique compared to other variational solvers is that the analysis can be performed directly in an axisymmetric cylindrical coordinate system. The two-dimensional solver improves the computational efficiency and minimizes potential errors in mass conservation that arise when interpolating from a three-dimensional domain. Another distinguishing characteristic from other variational solvers is the use of a Galerkin approach, which is similar to the Fourier spectral transform but uses the cubic B-spline as a basis (Ooyama 2002). The disadvantage of the B-spline basis is that it is not orthogonal and therefore requires an extra matrix to obtain the spline coefficients, but this is a fair tradeoff with its other desirable characteristics. The basis is computationally efficient and continuously differentiable to second order, allowing for efficient, accurate interpolation to observation locations, flexible incorporation of boundary conditions, and high numerical accuracy of kinematic derivatives. The analysis is performed in a manner similar to the spectral transform method (Machenhauer 1979), transforming to and from the spline coefficients and physical space at each step of the cost function minimization. A more technical description of SAMURAI is given in appendix B.

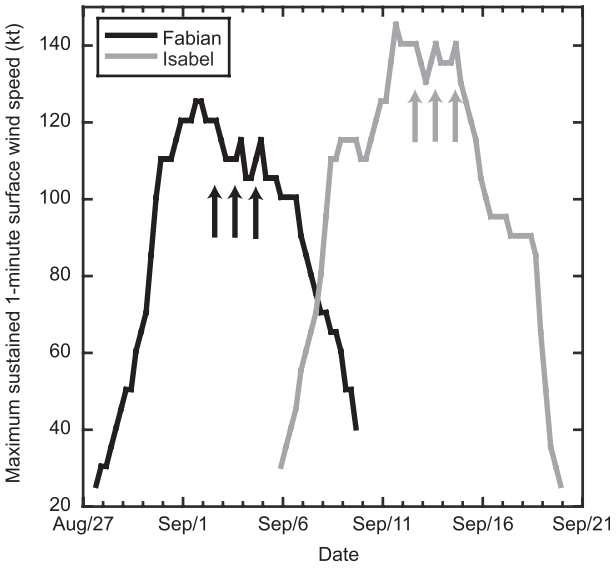

FIG. 2. NHC best-track intensity for Hurricanes Fabian (black line) and Isabel (gray line). The six intensive observing periods used in this study are highlighted on 2, 3, 4, 12, 13, and 14 September.

3. CBLAST data analysis

a. CBLAST dataset

Six intensive observing periods (IOPs) were conducted in Hurricane Fabian from 2 to 4 September and in Hurricane Isabel from 12 to 14 September 2003 as part of the CBLAST and National Oceanic and Atmospheric Administration (NOAA)/National Environmental Satellite, Data, and Information Service (NESDIS) Ocean Winds experiments (Black et al. 2007). NHC best-track intensities were estimated at greater than 120 kt (62 m s^{-1}) during the ~1600–2300 UTC time period in which observations were collected in Fabian and Isabel (Fig. 2), which makes both storms major hurricanes during the six IOPs. Two NOAA WP-3Ds (P3s), the NOAA G-IV, and United States Air Force C-130 aircraft collected in situ flight-level and dropsonde observations, with additional Doppler radar and stepped frequency microwave radiometer (SFMR) data obtained by the P3s only. The in situ dataset is similar to that used and described in detail in BM08. One of the advantages of a variational analysis is the ability to effectively combine different observations based on their individual error characteristics. The analysis composites were not found to be strongly sensitive to the magnitude of the prescribed errors, but the composites exhibited an unrealistic level of detail if the errors were too small. Observation errors

TABLE 2. Analysis times (UTC) for edited Doppler radar data for Fabian during 2–4 September and Isabel 12–14 September.

Fabian			Isabel		
2 Sep	3 Sep	4 Sep	12 Sep	13 Sep	14 Sep
1712–1726	1704–1714	1930–1949	1650–1659	1620–1642	1618–1646
1930–1941	1839–1849	2020–2035	1721–1726	1653–1709	1716–1730
1953–2002	1849–1857	2120–2139	1828–1846	1726–1742	1816–1830
2014–2027	1929–1939	2143–2159	1901–1910	1748–1807	1849–1902
2101–2114	1940–1950	2203–2219	1943–1948	1820–1841	1906–1919
2115–2123	2010–2020	2234–2250	2006–2019	1859–1913	1936–1947
2206–2219	2100–2110		2024–2036	1916–1930	1953–2009
2223–2235	2114–2124		2038–2049	1936–1950	2013–2029
2244–2252	2204–2211		2115–2130	1953–2007	2035–2050
				2026–2039	2052–2111
				2043–2055	2112–2125
				2102–2117	2130–2147
					2151–2207
					2209–2225

were set to 2 m s^{-1} for horizontal wind velocities, 2 g kg^{-1} for water vapor, 10 g m^{-3} for density, and 5 kJ for moist static energy. Vertical velocity errors were set to 2 m s^{-1} for flight level data and 4 m s^{-1} for dropsonde data.

The University of Massachusetts deployed a SFMR for measuring surface wind speed and rain rate on the NOAA-42 aircraft. The SFMR is a C-band (~5 cm) wavelength, downward-pointing radiometer that relates brightness temperatures at six different frequencies to surface emissivity and to empirically derived wind speeds. Since wind speed is a nonlinear observation operator, it was assumed here that the tangential velocity comprised the majority of the retrieved wind speed. If the surface inflow angle is less than 30°, then the error caused by this assumption is no more than about 12%. Given uncertainties in the calibration of the instrument at very high wind speeds and the simplification of the observation operator, the observation error was set to a relatively high value of 10 m s^{-1}. Nevertheless, these SFMR wind speed observations provided an important constraint on the surface wind speed when near-surface dropsonde winds were not available.

Doppler radar data result in a significant increase in both azimuthal and radial data density for the kinematic variables and add significant value to the analysis. The X-band (~3 cm) wavelength tail Doppler radar aboard the NOAA-42 aircraft employed a fore/aft scanning technique for all missions, which provided radial velocity data in a cone about 20° from the track both fore and aft of the aircraft. The data were first corrected

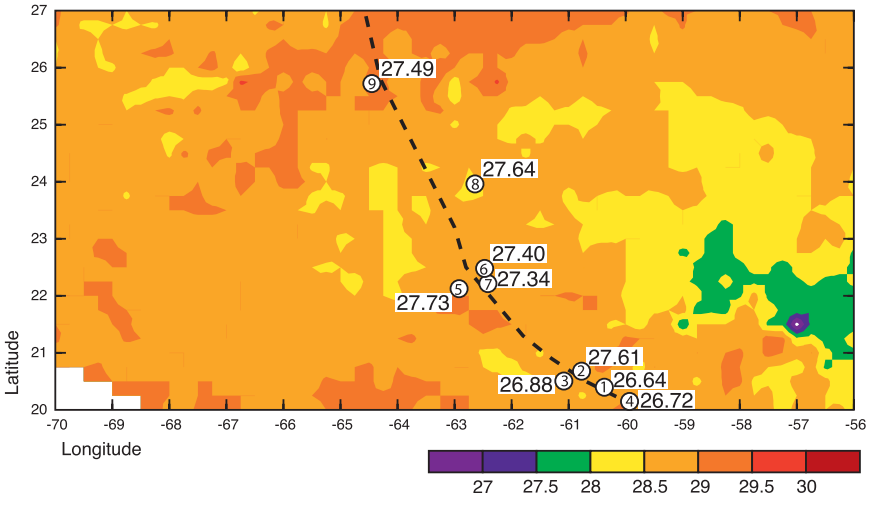

FIG. 3. SST derived from the TRMM Microwave Imager (average SST over 31 August–2 September; color) and AXBT data released into Hurricane Fabian. AXBT numbers correspond to Table 3. Track of Hurricane Fabian (dashed best track, 2–5 September) is shown for reference.

TABLE 3. SST observations (°C) for Hurricane Fabian.

AXBT No.	Time and date	AXBT SST	TMI SST	SST difference	Average SST	Analysis SST
1	1725:24 UTC 2 Sep	26.64	28.95	−2.31	27.795	
2	2002:29 UTC 2 Sep	27.61	28.65	−1.04	28.13	
3	2017:40 UTC 2 Sep	26.88	28.5	−1.62	27.69	
4	2049:46 UTC 2 Sep	26.72	28.8	−2.08	27.76	27.0
5	1712:06 UTC 3 Sep	27.73	28.95	−1.22	28.34	
6	1738:25 UTC 3 Sep	27.4	28.65	−1.25	28.025	
7	1915:23 UTC 3 Sep	27.34	28.65	−1.31	27.995	
8	2034:07 UTC 3 Sep	27.64	28.5	−0.86	28.07	27.5
9	1944:36 UTC 4 Sep	27.49	29.1	−1.61	28.295	28.0

for navigational errors and manually edited to remove ocean returns, radar side lobes, and other artifacts (Oye et al. 1995; Testud et al. 1995; Bosart et al. 2002). A large number of radial penetrations were edited for the current study, which included all of the multiple dropsonde releases. The times of the edited radar data used in the analysis are shown in Table 2. Most of these radial penetrations were used for circulation center fixes, but a few were too short to obtain meaningful center estimates. The Doppler data had an unambiguous radial velocity of less than 16 m s^{-1}, and frequently were aliased multiple times across the Nyquist interval because of the very high wind speeds. The Bargen and Brown (1980) algorithm was used to dealias the majority of the velocities using the in situ aircraft flight-level wind as a reference, but gaps and noise in the data required additional manual unfolding of many radar beams. The Doppler velocities were then averaged along each beam with a spatial resolution that approximately matched the diameter of the beam with increasing range, in order to reduce noise and the voluminous number of individual radar observations. The Doppler velocity error was assigned as the sum of the spectrum width of the velocity measurements (Keeler and Ellis 2000) plus an estimated error in the terminal fall speed of the precipitation, with a minimum error of 2 m s^{-1}.

b. Sea surface temperature

Direct measurements of the SST were made during the Hurricane Fabian missions by AXBTs released by the NOAA aircraft. A comparison of the AXBT temperatures and Tropical Rainfall Measuring Mission (TRMM) Microwave Imager (TMI) satellite estimates from the 3-day period prior to the first mission is illustrated in Fig. 3 and summarized in Table 3. The TMI-derived sea surface temperatures are near 28.5°C along the track throughout the analysis domain, but the AXBT temperatures are consistently 1°–2°C lower at the same locations. Since decreases of the SST are known to occur during and after the storm passage, the splash locations of the measurements were plotted in a storm-relative

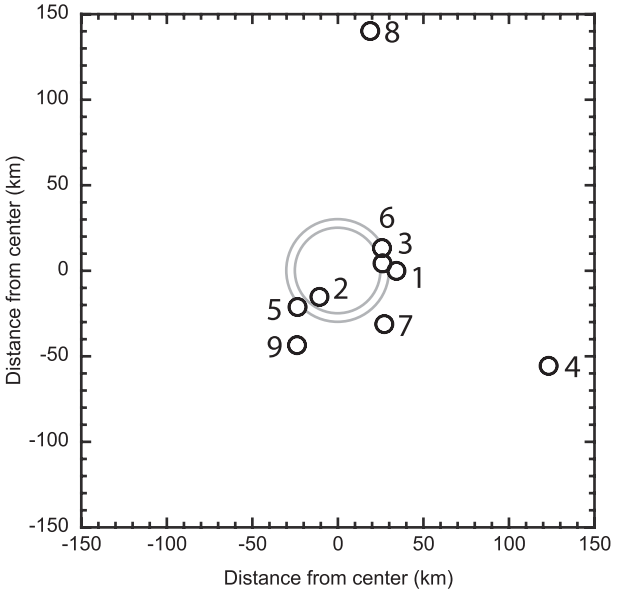

FIG. 4. Storm-relative AXBT splash locations. AXBT numbers correspond to Fig. 3. Gray annulus corresponds to approximate eyewall location at 30-km radius from the storm center.

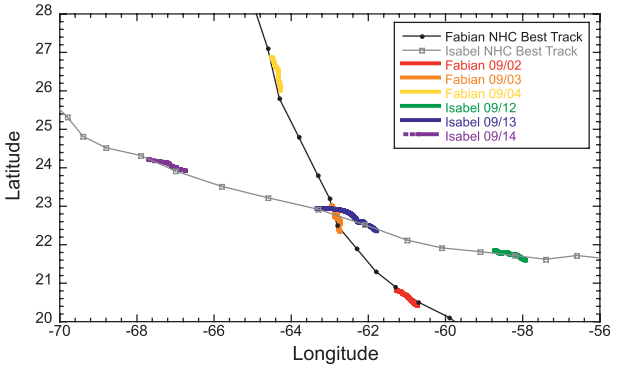

FIG. 5. NHC best tracks for Hurricanes Fabian (black line) and Isabel (gray line) and radar-derived tracks (color lines for Hurricanes Fabian and Isabel). Color lines indicate the analysis period for each aircraft mission used in this study (see inset).

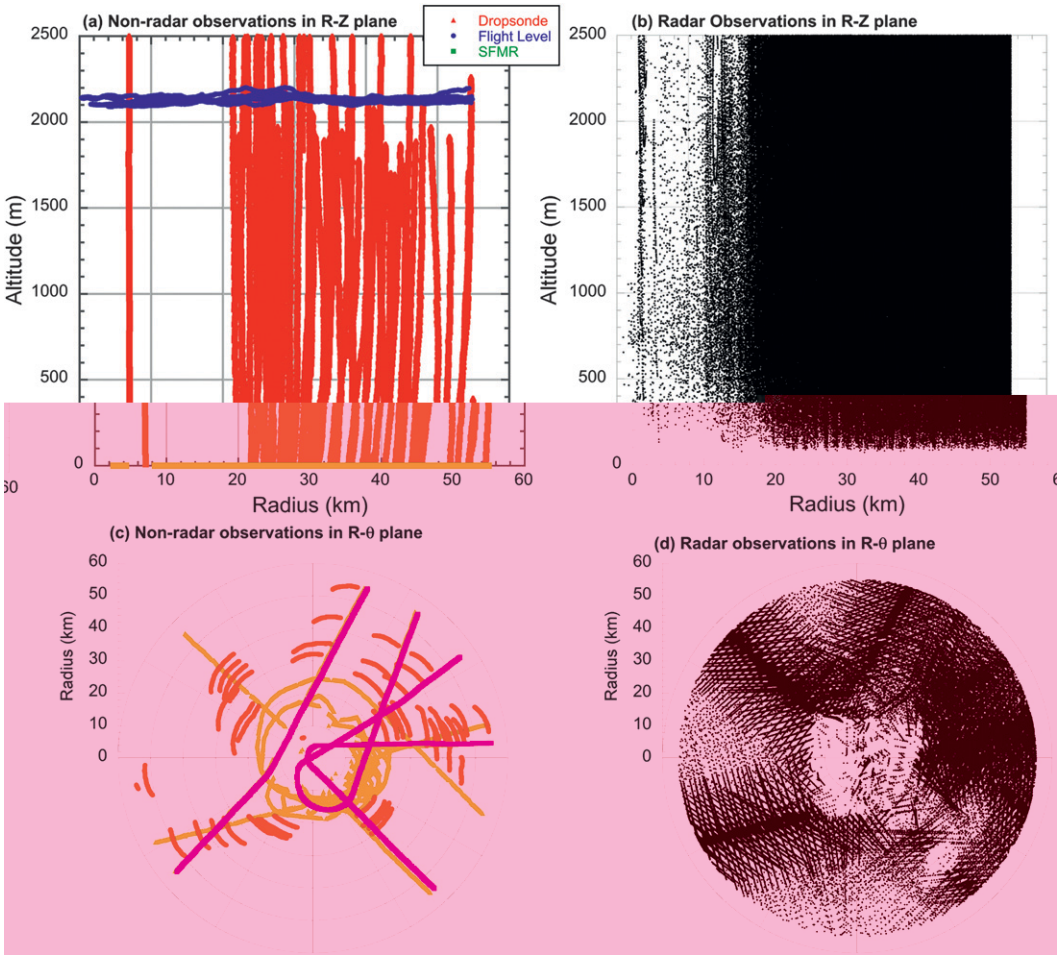

FIG. 6. Spatial distribution of observations from 2 September Hurricane Fabian missions. (a),(c) Nonradar and (b), (d) radar observations are plotted in the (a),(b) radius–height and (c),(d) radius–azimuth planes. Red triangles indicate dropsonde observations, blue circles indicate flight-level in situ observations, green squares indicate SFMR observations, and black dots indicate Doppler radar observations.

coordinate system (Fig. 4). All AXBT measurements were near the eyewall (gray annulus) with the exception of AXBTs 4 and 8. On 2 September, the two AXBTs on the right side of the eyewall are about 1°C lower than the one released on the left side. Given the relatively good azimuthal sampling around the eyewall, an average value of 27°C was chosen for this day. On 3 September, all of the AXBTs near the eyewall agree to within 0.4°C and are consistently 1.2°C lower than the TMI temperatures. A slightly higher value of 27.5°C was utilized on this day. It is interesting that the general location of Fabian on 3 September coincides with that of Isabel on 13 September. Since the SST is estimated at 27.5°C on both of these days, it appears that some of the ocean cooling that occurred during Fabian's passage recovered in the 10 days between the two storms. Only a single AXBT was available on 4 September, which was adjusted upward slightly to 28°C given the warmer SSTs derived from TMI.

A comprehensive analysis of the SST for the potential intensity estimates for Hurricane Isabel was performed by BM08 using satellite, buoy, and airborne radiometer measurements. Comparisons of the 3-day TMI microwave-derived product with the Advanced Very High Resolution Radiometer (AVHRR) infrared estimates are good, but given the high bias of the TMI estimates in the Fabian case, the 29°C on 14 September used in BM08 was adjusted downward slightly here to 28.5°C. The 28.5° and 27.5°C sea surface temperatures obtained previously for 12 and 13 September, respectively, were not modified.

c. *Circulation centers*

There are a variety of ways to define the center of a tropical cyclone, but an optimal center for the current study is one that minimizes aliasing associated with a truncated Fourier representation of the angular momentum

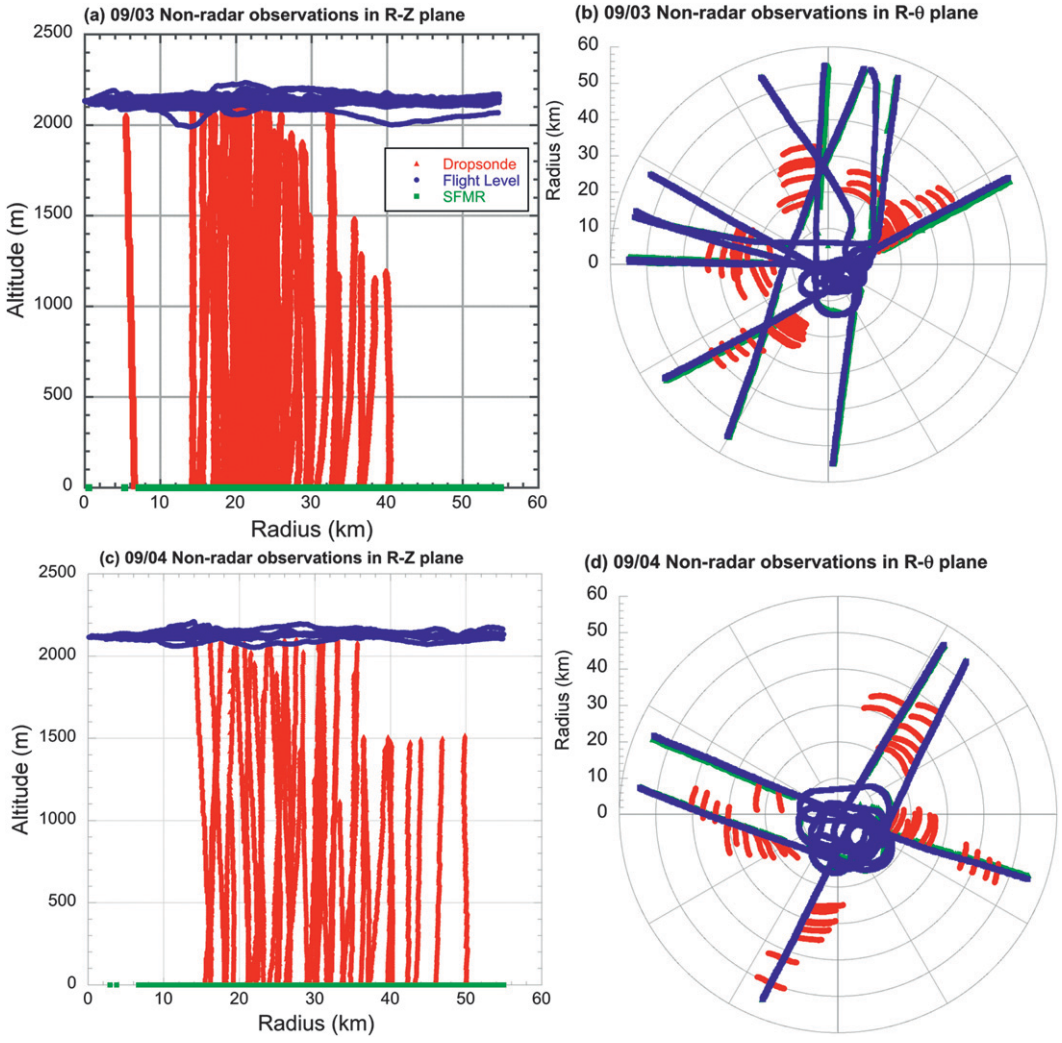

FIG. 7. Spatial distribution of nonradar observations from Hurricane Fabian missions on (a),(b) 3 and (c),(d) 4 September. Observations are plotted in the (a),(c) radius–height and (b),(d) radius–azimuth planes. Symbols are as in Fig. 6.

and total energy in azimuthal wavenumbers. The ''circulation center'' proposed by Marks et al. (1992) meets this criterion and is defined as the center that maximizes the axisymmetric tangential wind at the radius of maximum wind (RMW) derived from Doppler radar data. Since there is an inflection point in the radial gradient of tangential wind at the RMW, the circulation center also maximizes the vorticity at the RMW and the circulation inside the RMW. The circulation center maximizes the symmetric tangential wind by definition, and therefore minimizes aliasing onto higher-order azimuthal wavenumbers. The use of a broad swath of Doppler radar–derived wind data also helps to eliminate mesovortex centers that could be used mistakenly by analyzing only in situ data (Willoughby and Chelmow 1982).

To determine the circulation center, a two-dimensional ''simplex'' search (Nelder and Mead 1965) was used on a 1.5-km gridded dual-Doppler horizontal wind field (Mohr et al. 1986) to find the point that maximized the azimuthally averaged tangential wind in an annulus at a specified radius. Centers were deduced at 1-km altitude for each radial penetration of the airborne radar and interpolated over time using a cubic spline to create a high-resolution track. The track was reviewed and adjusted subjectively to remove outliers and centers biased by local wind maxima, with the accuracy of the derived high-resolution track estimated at about 3 km. The NHC best track and the high-resolution tracks derived from the simplex searches are shown for all six missions in Fig. 5. As expected, the tracks are nearly coincident, but the higher-resolution motion is apparent in the colored tracks. The largest discrepancy appears to be on 13 September, where the differences are likely due to the different

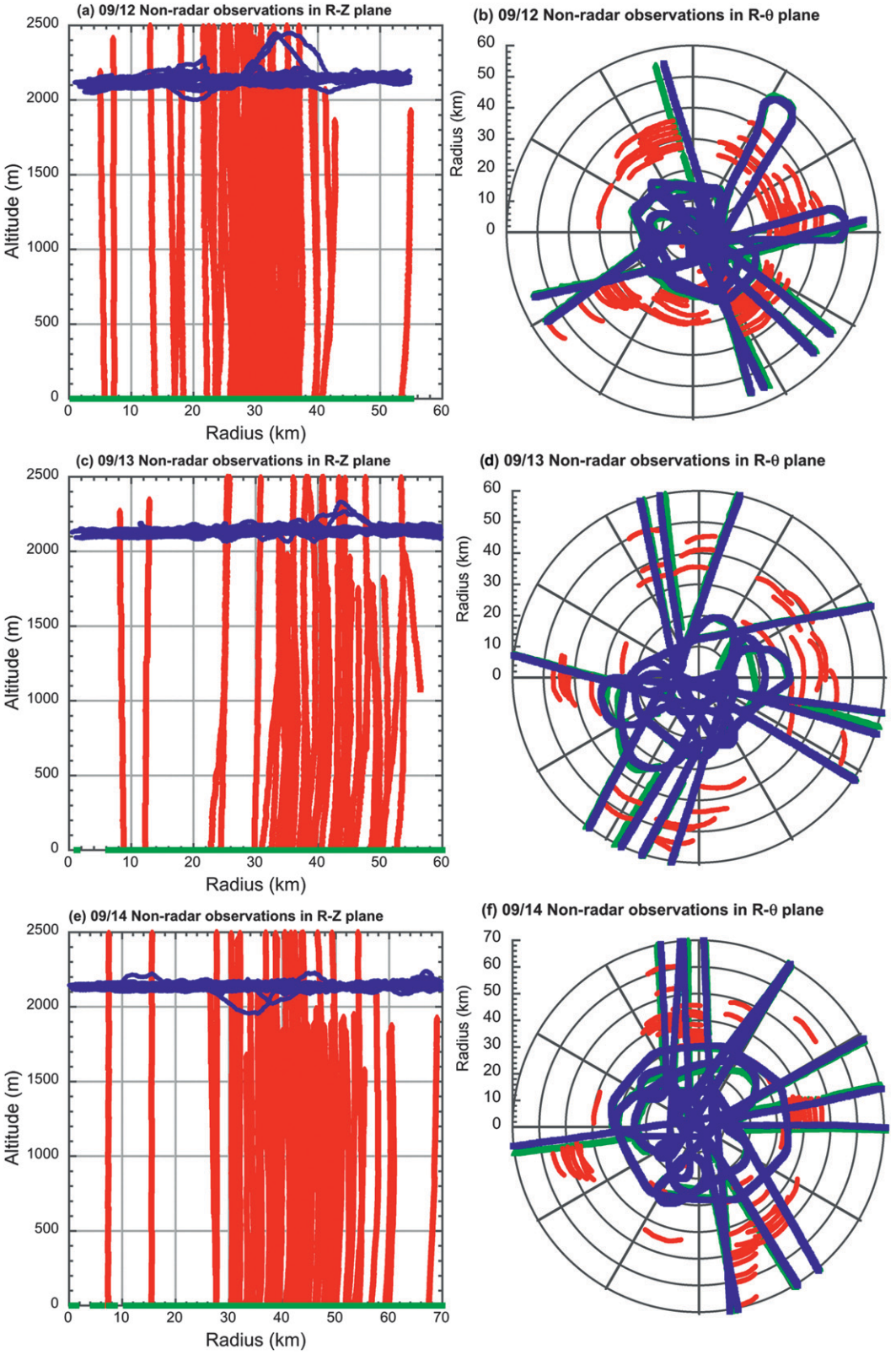

FIG. 8. Spatial distribution of nonradar observations from Hurricane Isabel on (a),(b) 12, (c),(d) 13, and (e),(f) 14 September. Observations are plotted in the (a),(c),(e) radius–height and (b)(d),(f) radius–azimuth planes. Symbols are as in Fig. 6.

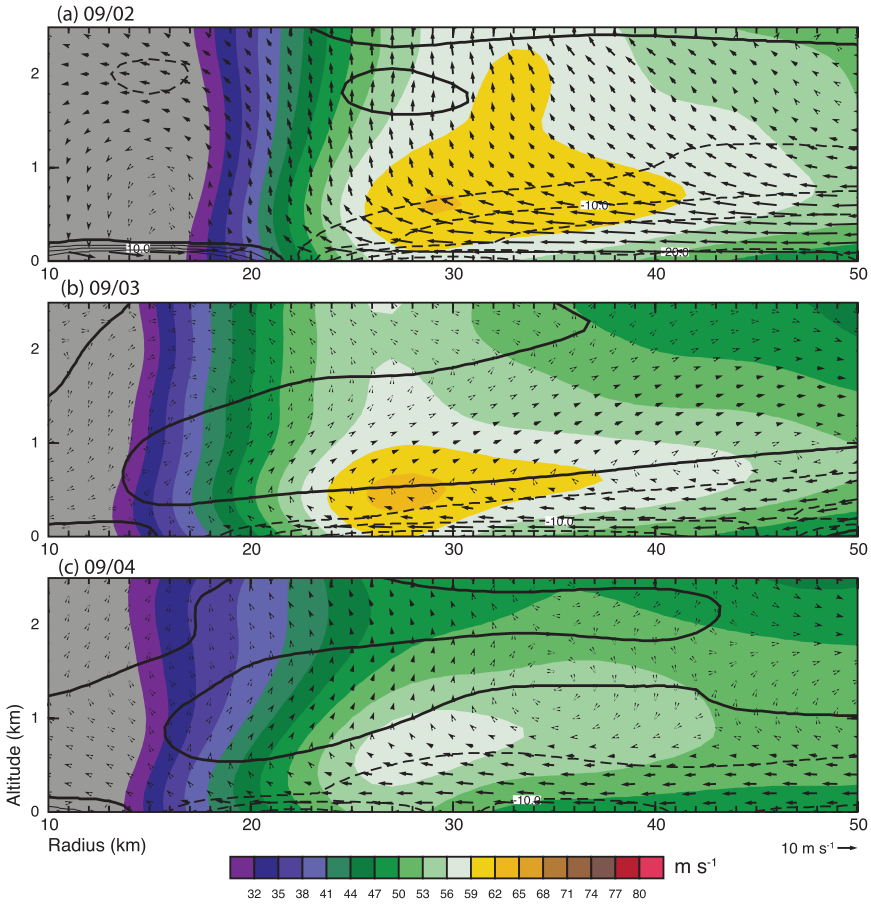

FIG. 9. Hurricane Fabian axisymmetric tangential wind (color), radial wind (5 m s^{-1} contours), and secondary circulation (vectors) from 2 to 4 September. Dashed contours indicate inflow and solid contours indicate outflow.

center definitions, but are still well within the large eye on this day.

d. SAMURAI

The SAMURAI technique was conducted for the six CBLAST missions using the data sources and circulation centers described above. The radar and nonradar observation data distribution for the 2 September mission is shown in Fig. 6 in both the radius–height and polar planes. It is clear that the radar data dominate the spatial distribution because of the wide swath of the tail Doppler radar. Comprehensive radar coverage provides good confidence in the kinematic fields throughout the domain, except near the eye where scatterers are limited. Excellent dropsonde coverage is also obtained in the main eyewall region near the RMW, with bracketing observations at flight level and at the surface from the SFMR. Good azimuthal sampling was achieved by the multiple sequences across the eyewall. Since only the flight level and dropsonde data provide thermodynamic data, the highest-quality energy analysis is limited to the ~20–50-km annulus. Since there are no high confidence a priori estimates of the structure available, other than the previous objective analysis with the same dataset, the data is only weakly constrained in poor data regions. By design of the CBLAST experiment, the data-rich regions coincide with the regions of highest wind speeds that are of interest for the current study.

The data distributions of nonradar observations for the remainder of the missions are shown in Figs. 7 and 8. Radar sampling was similar on all days to the first mission and is not shown. The dropsonde distributions are similar to the first mission, with limited data outside of 40-km radius but excellent azimuthal sampling on 3 September, and limited azimuthal sampling on 4 September. All of the Isabel missions are characterized by comprehensive radial and azimuthal sampling (Fig. 8). Note that distributions are slightly different from those shown in BM08 due to the use of radar-derived

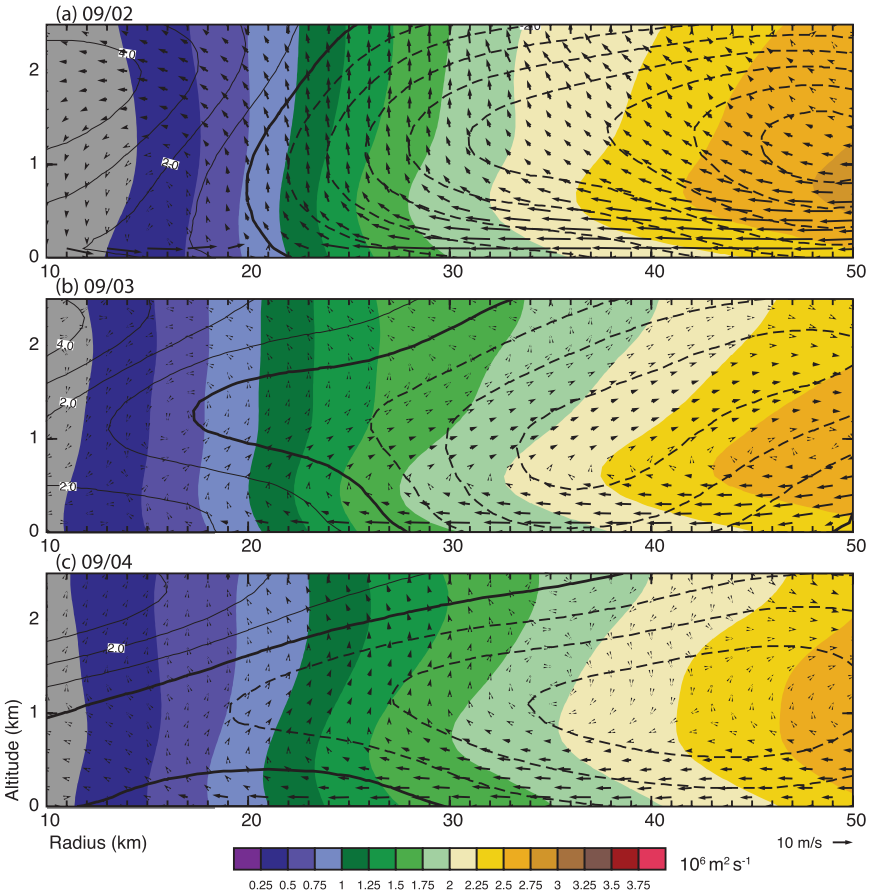

FIG. 10. Hurricane Fabian axisymmetric angular momentum (color), total energy (contours), and secondary circulation (vectors) from 2 to 4 September. The thick contour is 350 kJ kg^{-1}; solid lines and dashed lines indicate values above and below 350 kJ kg^{-1}, respectively, with a contour interval of 1 kJ kg^{-1}.

circulation centers instead of flight-level winds as described in section 3b, but the patterns are qualitatively the same. The number of observations included in each composite varies from about 500 000 to more than 1.7 million on 14 September (due to the large domain required to encompass the 45-km RMW). The difference between the observations and analysis yielded an approximately normal distribution with a mean and median near zero, linear correlations between the observations and analysis near 0.99, and linear slope and bias values near one and zero, respectively, for all days (not shown). The statistics indicate that the SAMURAI technique had high fidelity to the observations and suggest that the TCs were very azimuthally symmetric during all six missions.

The derived wind fields for Hurricane Fabian are shown in Fig. 9. The tangential winds depict a general weakening over the three analysis days, with a decrease in the depth of the strongest winds and slow weakening of the maximum tangential wind by the third day. The reduction in the depth and intensity of the tangential wind was concurrent with a reduction in the inflow depth and magnitude over the 3 days. The primary updraft appears to have weakened also during these 3 days. The RMW remained consistently just inside the 30-km radius, with a sharp gradient of tangential wind toward the center. Note that the low-level inflow continues past the RMW on all 3 days, with the flow turning upward near the high tangential wind gradient region. The absolute angular momentum M and total energy E are shown in Fig. 10. The secondary circulation generally follows the contours of M above the inflow layer, with more radially tilted M surfaces outside the RMW on the second and third days. The E contours depict also a toroidal shape that is similar to, but not congruent with, the M contours and secondary circulation. Note that the closed E contours at the outer radii (~50-km radius) are likely artifacts of the lack of data where the analysis relaxes

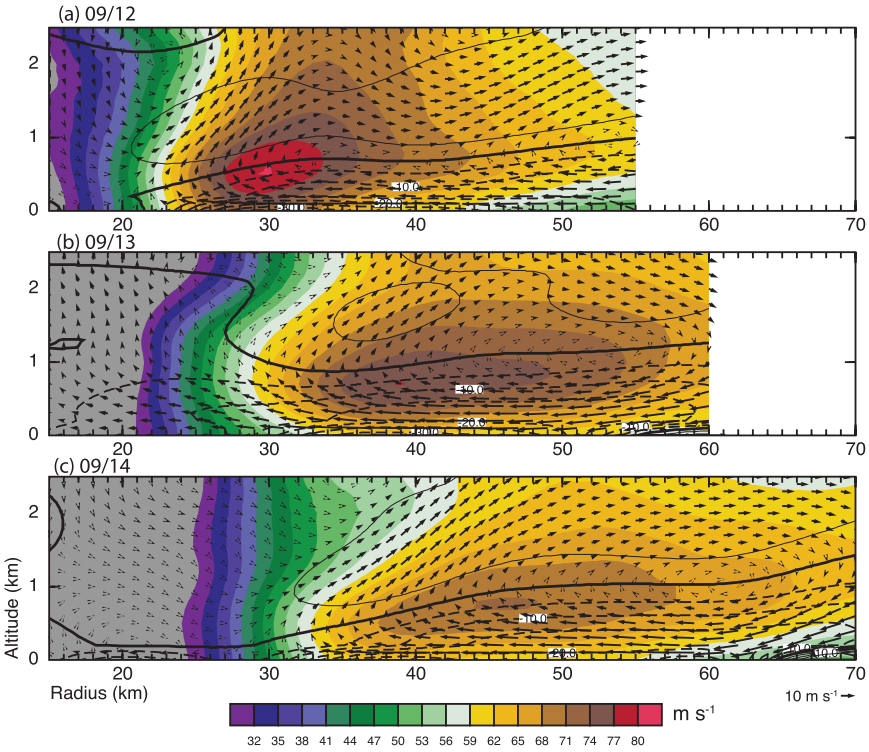

FIG. 11. Hurricane Isabel axisymmetric tangential wind (color), radial wind (5 m s^{-1} contours), and secondary circulation (vectors) from 12 to 14 September.

back to the prescribed reference state. Similarly, the thermodynamic structure inside of 20-km radius may be unreliable because of a data void. A reduced radial energy gradient is apparent on each consecutive day, which is consistent with the weakening trend in the kinematic variables.

The analyzed kinematic fields for Hurricane Isabel for all three missions are shown in Fig. 11. Note that the inner radius shown is 15 km for clarity because of the larger domain, although the analysis domain was extended to the TC center. The qualitative features of the SAMURAI technique are similar to the Barnes analysis used in BM08, but with enforced mass continuity of the secondary circulation and a notably sharper resolution of the boundary layer inflow. The characteristic ''overshoot'' of the inflow past the RMW is apparent during all three missions as was the case in the Fabian analysis, with a sloping inflow top that coincides with the height of the maximum tangential wind. A gradual weakening and expansion of the tangential wind as described in BM08 is evident, with a well-defined outflow and updraft core just above the maximum tangential wind on all 3 days. The absolute angular momentum and total energy analyses for Hurricane Isabel are shown in Fig. 12. The consistent structures of the secondary circulation, M, and E contours are similar to those in the analyses of Fabian. The total energy structure is also qualitatively similar to the moist entropy structure shown by BM08 (cf. their Fig. 5), as would be expected for similar thermodynamic variables.

The kinematic and thermodynamic structures apparent in the six analyses are consistent in their depiction of gradually weakening storms just past their peak intensity. The two different TCs and six different missions provide a good dataset for the flux retrievals, since the TCs were both in an approximate steady state but span 20 m s^{-1} in their peak tangential wind speeds and have slightly different RMW, total energy, and secondary circulation characteristics.

4. Air–sea fluxes

The absolute angular momentum and total energy budgets were resolved using the SAMURAI-derived axisymmetric composites shown in the previous section. A variety of control volumes was used to take into account the errors associated with the unresolved budget terms and quantitatively estimate the uncertainty in the derived fluxes. To determine the top of the control volume, traditional formalism for the planetary boundary layer assumes that the magnitude of the turbulent fluxes decreases to zero at the top of the mixed layer,

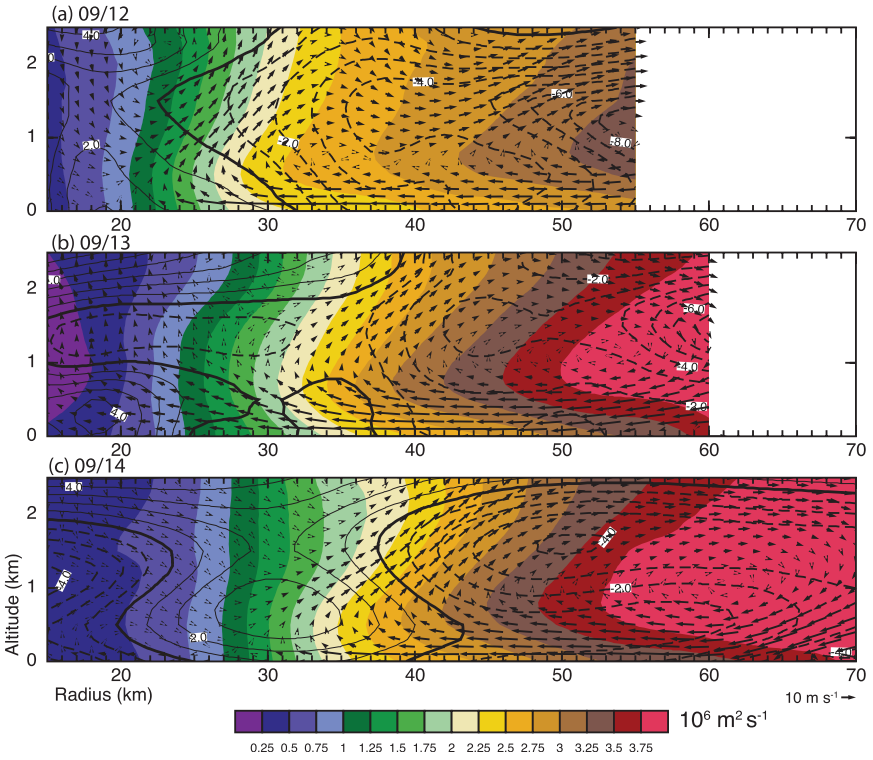

FIG. 12. Hurricane Isabel axisymmetric angular momentum (color), total energy (contours), and secondary circulation (vectors) from 12 to 14 September. The thick contour is 350 kJ kg^{-1}; solid lines and dashed lines indicate values above and below 350 kJ kg^{-1}, respectively, with a contour interval of 1 kJ kg^{-1}.

but the TCBL has a distinct separation of the boundary layer height defined mechanically and thermodynamically (Montgomery et al. 2006; Smith and Montgomery 2009; Zhang et al. 2011). In between the outer rainbands of Hurricanes Fabian and Isabel, the vertical momentum and humidity fluxes decreased to zero at 700 m, but the virtual potential temperature mixed layer depth was 400 m, and the inflow layer extended to 1 km (Zhang et al. 2009). Mixed layer depths and inflow heights are similar in the eyewall (Montgomery et al. 2006), but the TCBL may have different turbulence heights in the main updraft region compared with

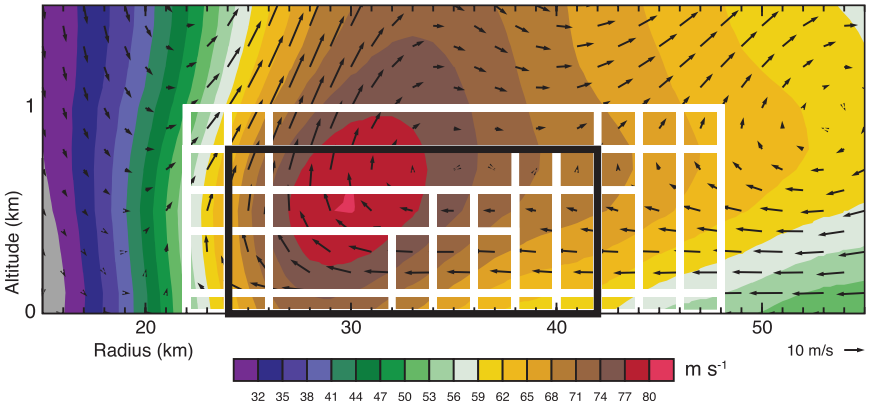

FIG. 13. Control volumes used for flux retrievals on 12 September. Tangential wind (color) and secondary circulation (vectors) are shown for reference. Thick white lines indicate the borders of overlapping control volumes. Small apparent boxes near the corners of the control volumes are artifacts resulting from the overlap. An example control volume is highlighted in black.

the inflow region outside the eyewall (Smith et al. 2008). Sensitivity tests suggested that volume tops below and near the top of the inflow layer were the most appropriate (appendix A), and a range of control volume depths from 400 to 1000 m was therefore utilized. Results with a fixed 1-km control volume top were within 10% and 20% of the mean C_D and C_K values over all volume depths, respectively.

The bottom of the control volume was set within the surface layer at either 10- or 100-m altitude. Variable control volume widths from 10 to 22 km were prescribed in 2-km increments, and the inner radius of the volume was varied by 2-km increments around a central value of 80% of the RMW. These volumes spanned the region in and around the eyewall, such that the average wind speed in the volume was always above 50 m s^{-1} for every mission. The aspect ratio (width divided by height) of all control volumes was between 20 and 30 as suggested by the sensitivity analysis. An illustration of the control volumes used on 12 September is shown in Fig. 13. The 72 white control volumes overlap throughout the eyewall region, with one of the example control volumes highlighted in black for clarity. Using multiple control volumes yielded a total of 72 flux ''samples'' per mission, representing a range of volume shapes, sizes, and locations centered around the RMW. The spectrum of control volumes adequately represents a reasonable statistical sample for obtaining a mean and standard deviation of the budget residual at the eyewall on each day.

The retrieved surface stress values are shown in Fig. 14a. Although considerable spread exists in the individual samples, a general agreement in the stress magnitudes is found with a mean value of 9.4 N m^{-2} and standard deviation of 4.6 N m^{-2}. A linear fit of the data has a correlation coefficient of 0.22 and only a slight upward trend with wind speed. Missions on 2 and 13 September have the highest stress but also two of the deepest inflow layers. The 14 September analysis has a deep inflow layer also, but with a stress more similar to the other missions. The retrieved stress on 12 September is low compared to the other missions. It is not clear that the low stress is due to physical differences on this day; it seems more likely that the scatter is due to inherent uncertainties in the methodology. Removing this mission from the sample improves the correlation coefficient to 0.53 and results in a more distinct upward trend with wind speed. The derived friction velocity is shown in Fig. 14b. The scatter is less than in the stress retrieval due to the square root dependence on the stress, with a mean value of 2.8 m s^{-1} and a 0.7 m s^{-1} standard deviation. These estimates indicate also a slight upward trend with wind speed with a correlation of 0.24, or 0.53 with the 12 September mission removed.

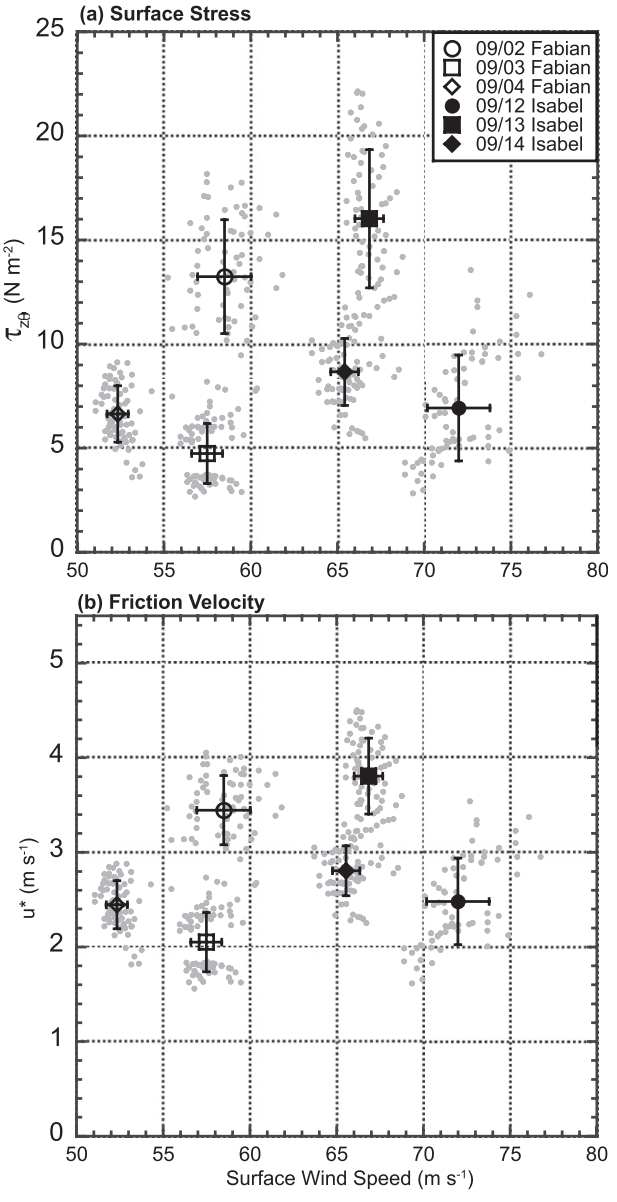

FIG. 14. (a) Derived surface stress and (b) derived friction velocity from the absolute angular momentum budget retrievals. Gray dots indicate individual samples from different control volumes, and large symbols indicate mean values from each research mission. Error bars indicate one standard deviation in derived quantity (vertical) and average surface wind speed (horizontal).

The retrieved surface enthalpy flux is shown in Fig. 15. These are the first known estimates of the enthalpy flux at wind speeds greater than 50 m s^{-1}, and likely the highest estimates of heat flux recorded over the ocean surface. There is less scatter than in the stress retrieval, and an increasing linear correlation with wind speed of 0.81. The increasing trend with wind speed is larger in the individual retrievals for each mission than in the mean, which may be due to the use of thinner control

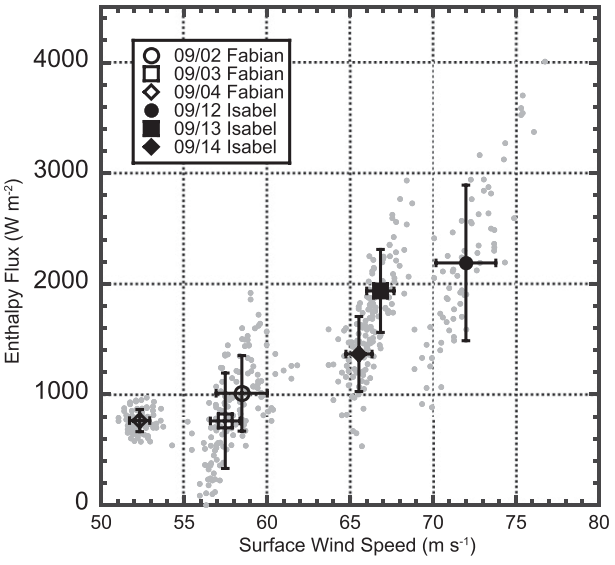

FIG. 15. Derived enthalpy flux from the absolute angular momentum and total energy budget retrievals. Symbols are as in Fig. 14.

volumes for the higher wind speeds. The wind speed dependence of the mean enthalpy flux from each mission increases from 764 W m^{-2} at 52 m s^{-1} to 2189 W m^{-2} at 72 m s^{-1}. The reasons for the reduced scatter and better correlation in the energy budget compared to the momentum budget are not apparent. It would appear that the derived thermodynamic structure was steadier on the ~6-h-mission time scale than the kinematic structure, but it is impossible to estimate the thermodynamic tendency with the current dataset.

The derived 10-m drag and enthalpy exchange coefficients are shown in Fig. 16. The C_K estimates show better agreement than the C_D estimates, as would be expected from better agreement of the enthalpy flux retrievals. The mean C_D is 2.4×10^{-3} with a standard deviation of 1.1×10^{-3}, which corresponds to about 46% uncertainty at the 67% confidence level and about 93% uncertainty at the 95% confidence level. The mean C_K is 1.0×10^{-3} with a standard deviation of 0.4×10^{-3}, which corresponds to about 40% uncertainty at the 67% confidence level and about 80% uncertainty at the 95% confidence level. These percentage uncertainties are consistent with a sensitivity analysis described in appendix A that indicated an approximately 50% standard deviation associated with the neglected budget terms. The C_D results do not indicate a significant dependence on wind speed, with a slightly decreasing linear correlation of only 0.11. The C_K results show a slight increase with wind speed, with a slope of 0.03 $(\text{m s}^{-1})^{-1}$ and a higher linear correlation of 0.53. Given the uncertainties and the weak slopes of both fits, there is no statistically significant change in either C_D or C_K in the wind speed range analyzed.

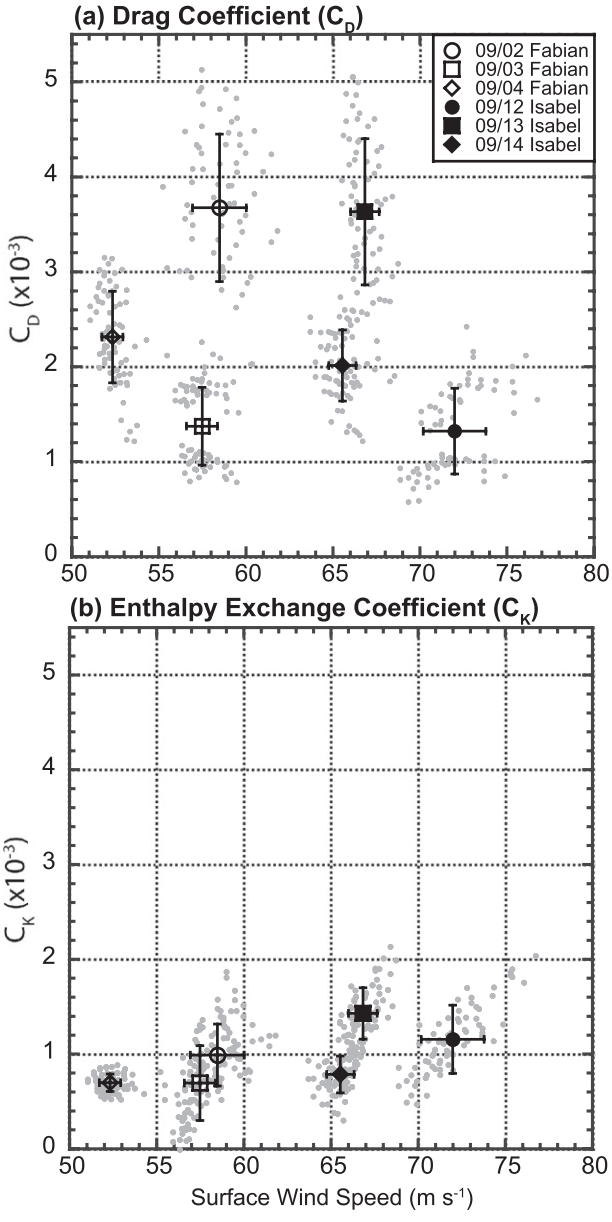

FIG. 16. Derived 10-m bulk exchange coefficients from the absolute angular momentum and total energy budget retrievals. Symbols are as in Fig. 14.

The histograms of the C_D and C_K samples shown in Fig. 17 suggest unimodal statistical distributions with some spread attributable to random errors. The statistical distributions are slightly skewed to the right (0.56 and 0.45 skewness for C_D and C_K, respectively), suggesting that the mean has a slight low bias compared to a normal distribution. Negative kurtosis (−0.58 and −0.12, respectively) indicates a rounder peak and shorter tails than a normal distribution. The cumulative probability distribution functions (CDFs; Fig. 17b) graphically

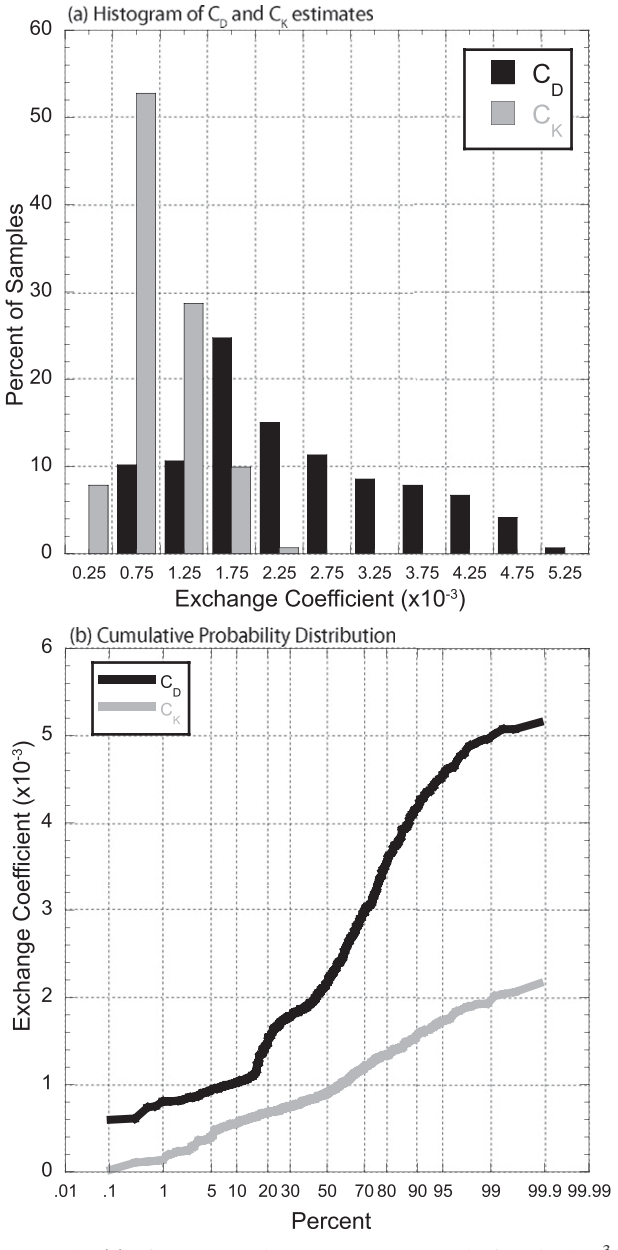

FIG. 17. (a) Histogram of the percentage of samples in 0.5×10^{-3} bins for C_D (black) and C_K (gray) for all retrievals. (b) Cumulative probability distributions for C_D (black) and C_K (gray) retrievals.

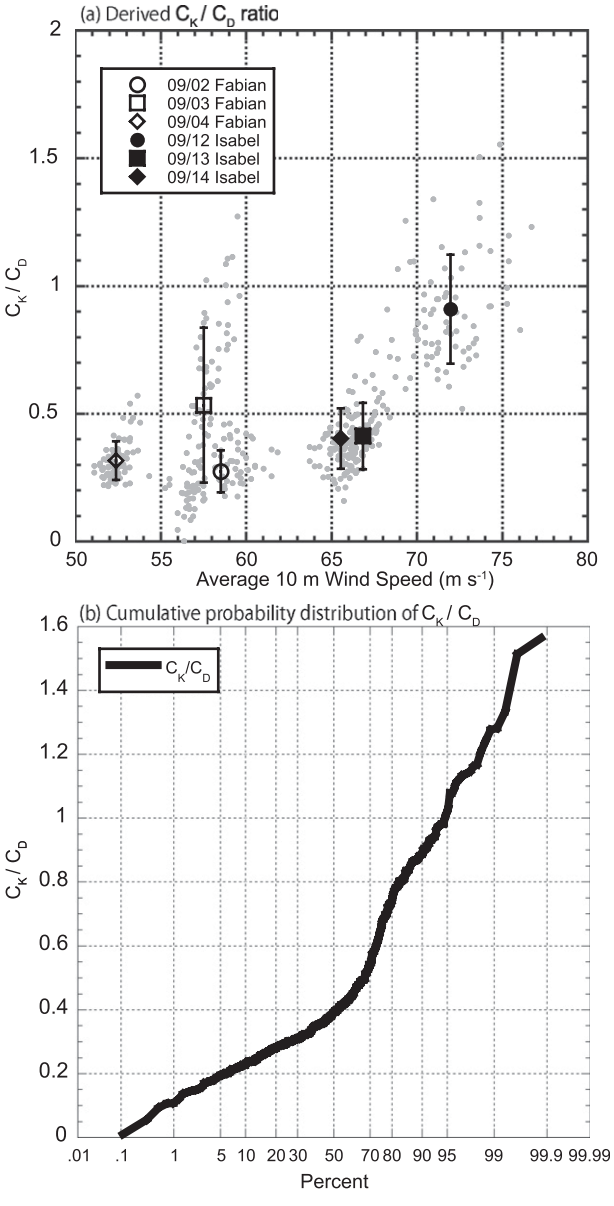

FIG. 18. (a) Ratio of C_K/C_D from budget retrievals. Symbols are as in Fig. 14. (b) Cumulative probability distribution for C_K/C_D retrievals.

illustrate the probability that the exchange coefficients are at or below a particular magnitude. These probabilities assume that the 432 samples obtained from varying the control volume over each of the six missions accurately represent samples from the true population distribution of exchange coefficient magnitudes. This assumption is based on the expectation that the variation of control volumes reasonably depicts the uncertainty associated with the unresolved budget terms, and that the remaining errors are random. The CDF for C_D has a steep slope above 1×10^{-3}, with 50%, 70%, and 90% probabilities that C_D is less than 2, 3, and 4×10^{-3}, respectively. The maximum estimated C_D is less than 5×10^{-3} with 99% probability, but this upper limit is not that useful given prior estimates and physical expectations. The slope of the CDF for C_K is much flatter than that of the corresponding slope for C_D. The maximum estimated C_K is less than 2×10^{-3} with 99% probability, with a 60% probability that the magnitude is less than 1×10^{-3}.

The ratios of C_k/C_D calculated from the different samples and the cumulative probability distribution are

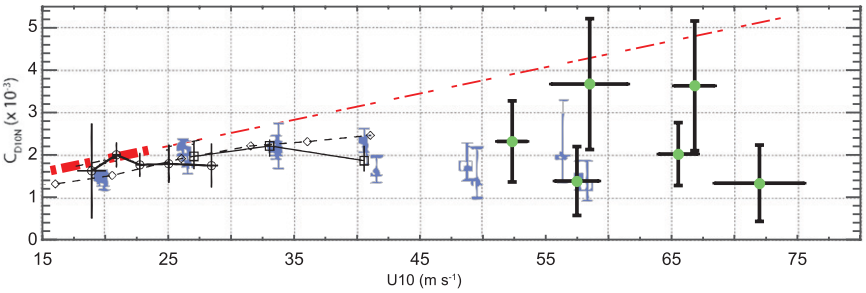

FIG. 19. Wind speed dependence of C_D from this study (green circles) compared with previous studies. Black symbols indicate data adapted from French et al. (2007) and blue symbols indicate data adapted from Vickery et al. (2009). Red line indicates measured (thick) and extrapolated (thin) Large and Pond (1981) drag coefficient.

shown in Fig. 18. With the exception of 12 September, the retrieved ratios are in relatively good agreement. Dividing the mean C_k/C_D gives an average ratio of 0.4, with a variation from 0.17 to 1.05 by adding and subtracting a single standard deviation of each coefficient in each direction. The mean value of all ratios calculated individually from each sample is 0.48 with a standard deviation of 0.27. A linear fit shows an increasing ratio with wind speed with a correlation of 0.58, but the increase is primarily due to the large ratios above 70 m s^{-1}. It is unclear why the 12 September mission appears to be an outlier, but this is probably due to unresolved budget terms as opposed to a significant change in the ratio above 70 m s^{-1}. It cannot be ruled out that C_D is reduced at these extreme wind speeds, but since C_k on 12 September agrees well with the other five cases, C_D derived for this day seems low. This discrepancy could be due to a potential eyewall replacement shortly after the aircraft mission (BM08), indicating a larger unresolved tendency term than on the other days. Even with the outlier ratio included, the cumulative probability distribution of all C_K/C_D ratios shown in Fig. 19b indicates an 80% probability that the ratio is less than 0.75, and a 93% probability that it is less than 1.0. Without the 12 September ratio these probabilities increase to 91% and 97%, respectively (not shown).

5. Summary and discussion

A budget methodology to retrieve air–sea fluxes of momentum and enthalpy was performed using data from six CBLAST missions into major hurricanes Fabian and Isabel (2003) at a range of surface wind speeds from 52 to 72 m s^{-1}. This study presents what are believed to be the first estimates of enthalpy fluxes (C_K) and the ratio of C_K/C_D in major hurricanes at wind speeds greater than 50 m s^{-1}. The results presented here also augment the limited surface stress and C_D estimates at these wind speeds. Several potential errors were identified by sensitivity analyses using simulated data and the errors were optimally mitigated to reduce the uncertainty of the estimates. The main sources of uncertainty identified were (i) unresolved budget terms, (ii) sea surface temperature errors, (iii) circulation center errors, and (iv) analysis errors. The "shear flux" term, representing the interaction of turbulent momentum fluxes and the mean shearing flow, was found to be important in the total energy budget and was included through an estimate of C_D obtained from the absolute angular momentum budget. Quantitative uncertainty estimates derived by varying the budget control volumes within the six different analyses are consistent with uncertainties estimated from sensitivity tests using simulated observations.

The mean C_D estimate for wind speeds above 50 m s^{-1} from this study is 2.4×10^{-3} with a standard deviation of 1.1×10^{-3}. Estimates of C_D from the current research are shown in Fig. 19 in relation to previous studies. The black symbols are adapted from French et al. (2007), where the black circles along the thick black line indicate the CBLAST estimates from that study, squares along the thin line indicate estimates from Powell et al. (2003), and diamonds along the thin dashed line indicate laboratory estimates from Donelan et al. (2004). The blue symbols are adapted from Vickery et al. (2009) showing the flux-profile estimates obtained from dropsondes. The current results are shown in green, along with 95% confidence intervals in black. The C_D estimates from this study are in general agreement with the previous studies that C_D does not continue to increase beyond about 30 m s^{-1}, though some increase cannot be strictly ruled out given the uncertainties in the estimates. At the 95% confidence level, the uncertainty does not preclude the possibility that the drag coefficient is near the extrapolated Large and Pond (1981) curve (dash-dotted curve), but the cumulative probability distribution indicates that the magnitude has a 90% probability of being less than 4×10^{-3}.

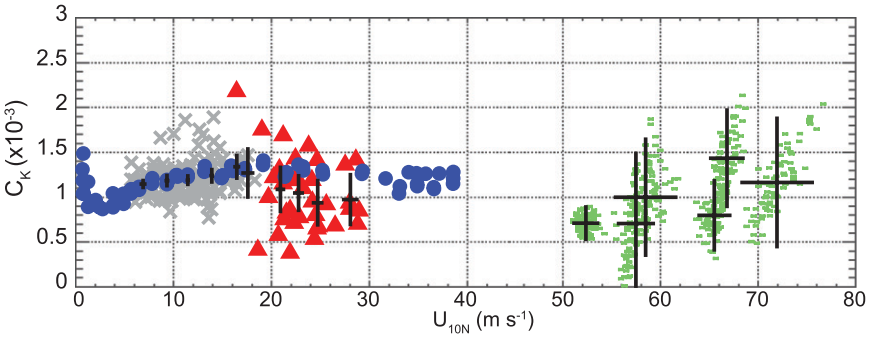

FIG. 20. Wind speed dependence of C_K from this study (green squares) compared with previous studies. ASIST laboratory results (blue circles) and CBLAST (red triangles) measurements shown with HEXOS results (gray crosses) adapted from Haus et al. (2010). The mean and 95% confidence intervals are shown in black.

The mean C_K estimate for wind speeds above 50 m s^{-1} from this study is 1.0×10^{-3} with a standard deviation of 0.4×10^{-3}. Estimates of C_K from the current research are shown in Fig. 20 with previous estimates. The current results are shown in green, along with Humidity Exchange over the Sea (HEXOS; DeCosmo et al. 1996; gray crosses), CBLAST (Zhang et al. 2008; red triangles), and laboratory results (blue circles) adapted from Haus et al. (2010). The mean and 95% confidence intervals for the HEXOS, CBLAST, and current results are indicated with black lines. The uncertainty at the 95% confidence level is higher in the current study compared to results from the other field experiments, but the envelope of C_K magnitudes is similar in all the field estimates. The uncertainties in C_K and C_D are similar in terms of a percentage error, but C_K has a lower uncertainty in terms of absolute error. There is a good linear correlation of the enthalpy flux with wind speed ($R = 0.81$; see Fig. 15) and the derived C_K is consistent across the different aircraft missions. A linear fit of C_K indicates a slight increase with wind speed above 50 m s^{-1}, but the increase is well within the uncertainty range and cannot be concluded definitively. The cumulative probability distribution indicates that C_K has an approximately 70% probability of being equal to or less than 1.2×10^{-3}, which is the approximate value determined at wind speeds greater than 15 m s^{-1}. These results suggest that it is probable that the magnitude of C_K is not dependent on wind speed in major hurricane conditions. Since the current results implicitly include the effects of sea spray, these results would also suggest that spray effects do not change C_K significantly. One hypothesis is that the spray flux has simply replaced the interfacial flux at these wind speeds (Haus et al. 2010), but the net enthalpy flux is similar. These results suggest also that sea spray parameterizations that increase C_K at high wind speeds may need revision (Bao et al. 2011; Andreas 2011). However, a partition between the spray and interfacial fluxes cannot be assessed by the current methodology.

The retrieved C_K/C_D ratios from the current research are shown with previous estimates in Fig. 21. These results indicate that the ratio is likely less than the 1.0 estimate derived by Emanuel (2003) at the ~28°C temperature range, and perhaps may be as low as 0.4.

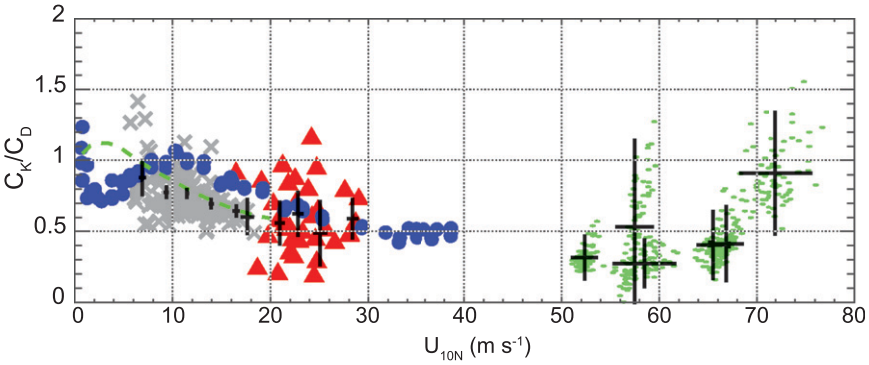

FIG. 21. Wind speed dependence of C_K/C_D from this study (green squares) compared with previous studies. Symbols are as in Fig. 20.

The results from this study do provide some support of the similarity hypothesis of Emanuel (2003) that C_D and C_K are constants at extreme wind speeds. The uncertainty in the coefficients and limited SST range precludes testing of the hypothesis that the C_K is SST dependent. These results suggest that the lower bound of the E-PI range for Hurricane Isabel presented in BM08 would be the most accurate (cf. their Fig. 1). These C_K/C_D estimates yield potential intensity estimates below 50 m s^{-1} without including dissipative heating. Recent studies suggest that these discrepancies between observations and E-PI theory may be largely due to gradient wind imbalance in the boundary layer (Smith et al. 2008; Bryan and Rotunno 2009). The current results are consistent also with recent three-dimensional numerical simulations that intensified to major-hurricane status with C_K/C_D ratios as low as 0.1 (Montgomery et al. 2010).

These new estimates of C_D and C_K may help to provide a basis to improve surface flux parameterizations, potential intensity theory, and our understanding of tropical cyclone intensity change. Although there is still considerable uncertainty in the magnitude of the air–sea fluxes and the corresponding bulk exchange coefficients in tropical cyclones, these estimates provide some new evidence that C_D and C_K do not increase at wind speeds above 50 m s^{-1}. Furthermore, the current results suggest that the C_K/C_D ratio does not change significantly from minor- to major-hurricane wind speeds. Additional observations of air–sea exchange at major-hurricane wind speeds are recommended to further reduce the uncertainty in these estimates.

Acknowledgments. The Office of Naval Research (ONR) provided the financial support for this research through Awards N0001407WR20290 and N001408WR 20129. We would like to acknowledge Peter Black, the Naval Research Lab, United States Air Force, National Oceanic and Atmospheric Administration, and ONR for organizing the CBLAST experiment and collecting the data used for this study. Thanks also go to Jeanne Davencens and William Ramstrom for their preliminary work related to this research, and Michael Bell's Ph.D. committee for their valuable comments and feedback on the research.

APPENDIX A

Error Analysis

To test the accuracy of the methodology used in this study, momentum and energy budget analyses were computed using idealized numerical simulations from the two-dimensional, axisymmetric hurricane model developed by Rotunno and Emanuel (1987, hereafter RE87) and the three-dimensional Advanced Research Weather and Forecasting Model version 3.0.1.1 (hereafter simply WRF). Details on the numerical configurations of the models are given in Bell (2010). The initial atmospheric condition used for both models was a thermodynamic background defined by the Jordan (1958) mean tropical Atlantic sounding modified to be in thermal wind balance (Smith 2006) with an analytic mesoscale vortex [RE87, Eq. (37)]. All simulations were approximately steady state after 144 h of integration time.

The accuracy of the methodology was evaluated by comparing the retrieved exchange coefficients from simulated observations with known exchange coefficients derived from the numerical simulations. One WRF simulation and five RE87 simulations were performed with varying exchange coefficients. A capped roughness length of 2.85×10^{-3} m and fixed moisture roughness length of 1×10^{-6} m were used in the WRF simulation to approximately match the derived magnitudes of C_D and C_K from this study. A variety of exchange coefficient values were prescribed explicitly through bulk aerodynamic formulas in the RE87 simulations. Initial tests indicated that the fluxes and exchange coefficients could be retrieved exactly from the simulations with all budget terms included and no observational errors (not shown). Estimates of errors in the derived exchange coefficients using real observations were calculated by subsequently neglecting residual budget terms [Eqs. (4) and (8)] and also by adding errors to the simulated observations. It must be noted that some error was introduced by temporal averaging and interpolating the data from the staggered to unstaggered model grids, and in the WRF case by azimuthally averaging. The interpolation led to nonnegligible errors in axisymmetric mass continuity, which required correction by adjusting w through a vertical integration of the mass continuity equation on the temporally averaged, unstaggered grids.

An example of the retrieved C_D and C_K from the simulated observations with the residual budget terms neglected and no observational errors is shown in Fig. A1. The results are from model output averaged over eight "missions" of 6-h duration from 144 to 192 h, using control volumes similar to those used with the real observations. One standard deviation from the mean C_D and C_K from the eight synthetic missions is indicated by the vertical bars. The retrieval methodology is able to reasonably distinguish between different values of the exchange coefficients from the six different simulations, with differences from the actual magnitudes on the order of 50% or lower.

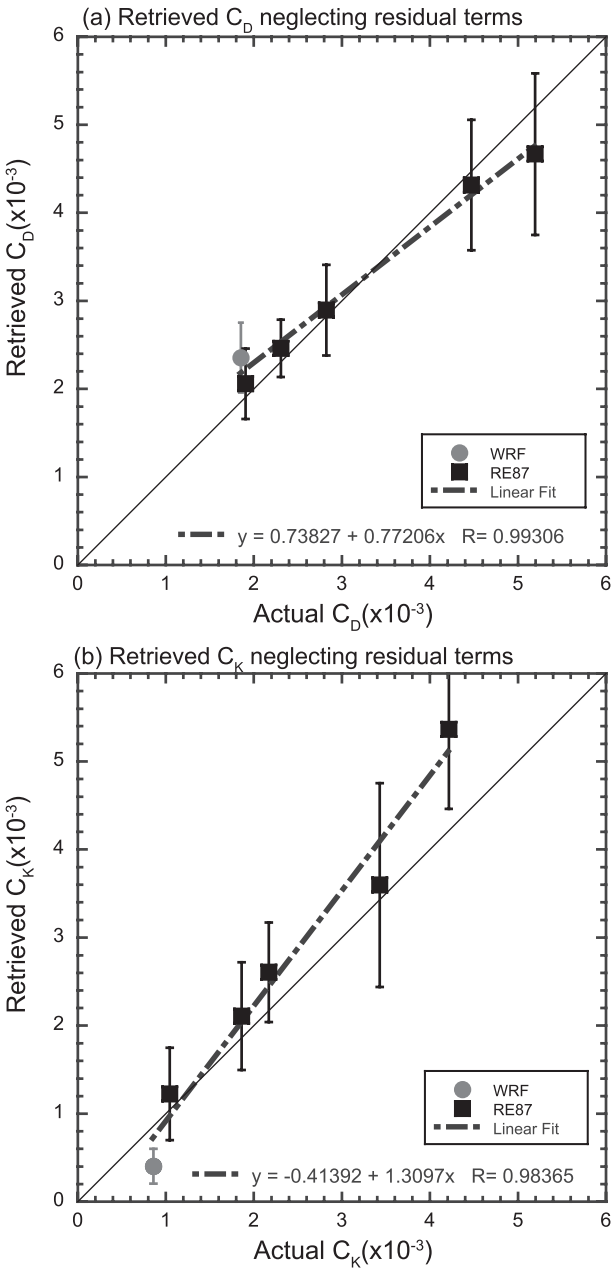

FIG. A1. Retrieved exchange coefficients vs known coefficients from synthetic observations after neglecting budget residual terms. Gray circles indicate WRF retrievals, and black squares indicate RE87 retrievals. Dashed gray line indicates linear fit of the data, with the linear coefficients and correlation at the bottom of each panel. Error bars indicate one standard deviation in the retrieved quantity.

SST errors were assessed in a straightforward manner by adding error to the SSTs from the model simulations during the C_K retrievals. Errors in the SST were approximately linearly correlated with errors in the retrieved C_K of about 20% °C^{-1}. We estimate the uncertainty in the SST estimates derived from the satellite imagery and AXBTs to be on the order of 1°C or less, yielding a C_K uncertainty of ±20% from this error source.

Center errors were assessed by repositioning the observations and reprojecting the wind components in a cylindrical coordinate system displaced from the known center. The largest error was found to result from the reprojection of tangential wind to apparent radial wind. For example, a 5-km displacement of a 60 m s^{-1} tangential wind at 20-km radius can yield up to a 15 m s^{-1} error in the radial wind velocity. Integrating a radial velocity error weighted by mass, radius, and total energy or absolute angular momentum can result in a large error in the resolved flux across the boundary of the control volume. Radial velocity errors arising from center displacement change with radius, which also introduces divergence errors that affect vertical motion and the resolved flux through the top of the control volume. When using only a single radial pass for the retrieval, errors resulting from center displacements can yield up to a ±25% error in the retrieved exchange coefficients per kilometer of displacement. If the center errors are random, however, then temporal averaging will mitigate errors in the analyzed wind components. The CBLAST analyses were therefore averaged over multiple radial passes over approximately 6-h periods to minimize this error. The temporal averaging reduces the estimated uncertainty in the retrieved C_D and C_K to about 20% for up to 3-km average center errors.

Analysis errors were assessed by comparing retrievals using SAMURAI on the simulated observations with small random observational errors. This yielded less than 20% error in the retrieved fluxes compared to using the interpolated model data directly. The retrievals were not overly sensitive to the exact magnitude of the surface winds used to convert the retrieved surface layer fluxes to bulk exchange coefficients compared to other analysis errors. The estimated bulk Richardson number was near zero because of the strong vertical wind shear in the analyzed cases; therefore, no stability corrections were made to explicitly adjust the exchange coefficients to neutral stability. Uncertainties in the surface wind derived from the dropsonde and SFMR data and departures from neutral stability are therefore included in the 20% estimate.

Errors in the resolved fluxes are compounded by integration over the depth and width of the budget control volume. This suggests that thinner, shallower control volumes would be prone to less numerical error, but physical constraints and the data distribution must be considered also. Optimal control volumes were somewhat different using the RE87 and WRF simulated observations. The WRF simulations suggested an optimal depth of 400 m, but the RE87 simulations suggested a deeper volume. Sensitivity tests with the simulated

observations indicated that aspect ratios of 20–30 (width divided by height) yielded the least error in the retrieved C_D and C_K from both the RE87 and WRF simulations. Because of uncertainties in the simulations, the minimum depth of the control volume was largely determined by our expectation that the unresolved vertical eddy fluxes are small near the top of the boundary layer. Wider control volumes yield a larger integrated surface flux that is more tolerant to errors in the neglected residual terms, but are limited in maximum width by the data distribution. Therefore, a compromise was struck between physical and numerical constraints on the size of the control volume. A set of 72 control volumes was constructed for each mission to maintain an optimal aspect ratio while also preserving the physical and data distribution constraints.

APPENDIX B

SAMURAI Technique

The analysis uses an incremental form of the variational cost function that avoids the inversion of the background error covariance matrix by using a control variable $\hat{\mathbf{x}}$, similar to the forms in Barker et al. [2004, Eq. (2)] and Gao et al. [2004, Eq. (7)]:

$$J(\hat{\mathbf{x}}) = \frac{1}{2}\hat{\mathbf{x}}^{\mathrm{T}}\hat{\mathbf{x}} + \frac{1}{2}(\mathbf{HC}\hat{\mathbf{x}} - \mathbf{d})^{\mathrm{T}}\mathbf{R}^{-1}(\mathbf{HC}\hat{\mathbf{x}} - \mathbf{d}), \qquad \text{(B1)}$$

where $\mathbf{H}$ denotes the linearized observation operator, $\mathbf{C}$ denotes the square root of the background error covariance matrix, $\mathbf{R}$ denotes the observation error covariance matrix, and $\mathbf{d} \equiv \mathbf{y} - h(\mathbf{x}_b)$ denotes the difference between the observations $\mathbf{y}$ and the nonlinear observation operator applied to the background state estimate $h(\mathbf{x}_b)$. In the current study, h and $\mathbf{H}$ are equivalent. The cost function is minimized using a conjugate gradient algorithm (Polak 1971; Press et al. 2002) to find the atmospheric state where the gradient with respect to $\hat{\mathbf{x}}$ is 0:

$$\nabla J(\hat{\mathbf{x}}) = (\mathbf{I} + \mathbf{C}^{\mathrm{T}}\mathbf{H}^{\mathrm{T}}\mathbf{R}^{-1}\mathbf{HC})\hat{\mathbf{x}} - \mathbf{C}^{\mathrm{T}}\mathbf{H}^{\mathrm{T}}\mathbf{R}^{-1}\mathbf{d}. \qquad \text{(B2)}$$

We can express the transform from the control variable to an analysis increment as an operator sequence $\delta\mathbf{x} = \mathbf{C}\hat{\mathbf{x}} = \mathbf{SDF}\hat{\mathbf{x}}$. The $\mathbf{SDF}$ matrix transforms represent the cubic B-spline transform, standard deviation of the background error, and recursive filter operators, respectively. For brevity, only the one-dimensional transform for the radial direction is illustrated here. An additional transformation in the z direction follows. The spline transform $\mathbf{S}$ is given by

$$\begin{aligned}
&\mathbf{S} = (\mathbf{P} + \mathbf{Q})^{-1},\\
&\mathbf{P} = [p_{mm'}]^{\mathrm{T}}, \quad p_{mm'} = \int_D \phi_m(r)\phi_{m'}(r)\,dr,\\
&\mathbf{Q} = [q_{mm'}]^{\mathrm{T}}, \quad q_{mm'} = \int_D \epsilon_q(r)\phi'''_m(r)\phi'''_{m'}(r)\,dr,\\
&\phi_m(r) = \Phi\left(\frac{r - r_m}{\Delta r}\right), \quad \text{for} \quad m \in M \quad \text{and} \quad r \in D,
\end{aligned} \qquad \text{(B3)}$$

where Φ is the cubic B-spline given by

$$\begin{aligned}
\frac{1}{6}(2 - |\xi|)^3 - \frac{2}{3}(1 - |\xi|)^3 \quad &\text{if} \quad 1 \geq |\xi| \geq 0,\\
\frac{1}{6}(2 - |\xi|)^3 \quad &\text{if} \quad 2 \geq |\xi| \geq 1,\\
0 \quad &\text{if} \quad |\xi| \geq 2.
\end{aligned} \qquad \text{(B4)}$$

Note that $\mathbf{P}$ becomes the identity matrix for orthogonal basis functions, but is required for computing the cubic B-spline coefficients. Here $\mathbf{Q}$ is a third derivative constraint to reduce Gibb's oscillations in the spline transform (Ooyama 2002), with ϵ_q being a specified effective spatial filter cutoff length. The resulting increment or analysis can then be evaluated at any point in the physical domain through the inner product of the basis functions and the spline coefficients. For example, for the radial wind

$$u(r) = \phi^{\mathrm{T}}\mathbf{x} + \tilde{\phi}^{\mathrm{T}}\tilde{\mathbf{x}}, \qquad \text{(B5)}$$

where the second term on the right-hand side represents imposed boundary conditions (Ooyama 2002).

For the current study, the background error correlations were assumed to be Gaussian and isotropic, and were calculated using an efficient recursive filter operator that replicates the effects of this correlation (Purser et al. 2003). The operator combination $\mathbf{DF}$ is the application of the background error covariance matrix, where $\mathbf{D}$ is the standard deviation of the background errors and $\mathbf{F}$ is the recursive filter. The standard deviation of the background errors was purposefully set very high given no prior knowledge of background state other than the objective analysis from BM08. A large background error standard deviation has the detrimental side effect of making the spline analysis unconstrained in data-poor regions. The recursive filter length scale acts both as an effective distance for the influence of the observations and as a spatial filter. A large length scale helps spread the information provided by an observation across data gaps but also removes finescale detail from the analysis. Sensitivity tests indicated that a 6Δ background error

length scale (where Δ is the horizontal or vertical grid scale) was a good compromise between smoothing and data density constraints, and was adequate for the current study.

The control variable state vector is constructed in axisymmetric cylindrical space and is given by $\mathbf{x} = \{\rho rv, \psi, S', q', \rho_a'\}^{\mathrm{T}}$, where ρ denotes the moist density including water vapor, ψ denotes the transverse streamfunction, S denotes the moist static energy ($c_pT + Lq + gz$), ρ_a denotes the dry air density, primes represent departures from a static background reference state, and the remaining symbols are as defined in section 2a. The mean tropical sounding from Jordan (1958) was used as the reference state in this study. Radial and vertical momentum were recovered from the streamfunction using $\rho u = -\partial\psi/\partial z$ and $\rho w = \partial\psi/\partial r$. The vertical and radial resolutions of the analyses used in the study were 100 m and 1 km, respectively.

REFERENCES

Andreas, E., 2011: Fallacies of the enthalpy transfer coefficient over the ocean in high winds. *J. Atmos. Sci.,* **68,** 1435–1445.

Bao, J.-W., S. A. Michelson, and J. M. Wilczak, 2002: Sensitivity of numerical simulations to parameterizations of roughness for surface heat fluxes at high winds over the sea. *Mon. Wea. Rev.,* **130,** 1926–1932.

——, C. W. Fairall, S. A. Michelson, and L. Bianco, 2011: Parameterizations of sea-spray impact on the air–sea momentum and heat fluxes. *Mon. Wea. Rev.,* **139,** 3781–3797.

Bargen, D. W., and R. C. Brown, 1980: Interactive radar velocity unfolding. Preprints, *19th Conf. on Radar Meteorology,* Miami Beach, FL, Amer. Meteor. Soc., 278–285.

Barker, D. M., W. Huang, Y.-R. Guo, A. Bourgeois, and Q. N. Xiao, 2004: A three- dimensional variational data assimilation system for MM5: Implementation and initial results. *Mon. Wea. Rev.,* **132,** 897–914.

Barnes, S. L., 1973: Mesoscale objective analysis using weighted time-series observations. NOAA/National Severe Storms Laboratory Tech. Memo. ERL NSSL-62, 60 pp.

Bell, M. M., 2010: Air–sea enthalpy and momentum exchange at major hurricane wind speeds. Ph.D. thesis, Naval Postgraduate School, 147 pp. [Available online at http://edocs.nps.edu/npspubs/scholarly/dissert/2010/Jun/10Jun_Bell_PhD.pdf.]

——, and M. T. Montgomery, 2008: Observed structure, evolution, and potential intensity of category 5 Hurricane Isabel (2003) from 12 to 14 September. *Mon. Wea. Rev.,* **136,** 2023–2046.

Black, P. G., R. W. Burpee, N. M. Dorst, and W. L. Adams, 1986: Appearance of the sea surface in tropical cyclones. *Wea. Forecasting,* **1,** 102–107.

——, and Coauthors, 2007: Air–sea exchange in hurricanes: Synthesis of observations from the Coupled Boundary Layer Air–Sea Transfer experiment. *Bull. Amer. Meteor. Soc.,* **88,** 357–374.

Bosart, B. L., W.-C. Lee, and R. M. Wakimoto, 2002: Procedures to improve the accuracy of airborne Doppler radar data. *J. Atmos. Oceanic Technol.,* **19,** 322–339.

Braun, S. A., and W.-K. Tao, 2000: Sensitivity of high-resolution simulations of Hurricane Bob (1991) to planetary boundary layer parameterizations. *Mon. Wea. Rev.,* **128,** 3941–3961.

Bryan, G. H., and R. Rotunno, 2009: The maximum intensity of tropical cyclones in axisymmetric numerical model simulations. *Mon. Wea. Rev.,* **137,** 1770–1789.

Davis, C., and Coauthors, 2008: Prediction of landfalling hurricanes with the Advanced Hurricane WRF model. *Mon. Wea. Rev.,* **136,** 1990–2005.

DeCosmo, J., K. B. Katsaros, S. D. Smith, R. J. Anderson, W. A. Oost, K. Bumke, and H. Chadwick, 1996: Air-sea exchange of water vapor and sensible heat: The Humidity Exchange over the Sea (HEXOS) results. *J. Geophys. Res.,* **101,** 12 001–12 016.

Donelan, M. A., B. K. Haus, N. Reul, W. J. Plant, M. Stianssnie, H. C. Graber, O. B. Brown, and E. S. Saltzman, 2004: On the limiting aerodynamic roughness of the ocean in very strong winds. *Geophys. Res. Lett.,* **31,** L18306, doi:10.1029/2004GL019460.

Drennan, W. M., J. A. Zhang, J. R. French, C. McCormick, and P. G. Black, 2007: Turbulent fluxes in the hurricane boundary layer. Part II: Latent heat flux. *J. Atmos. Sci.,* **64,** 1103–1115.

Emanuel, K. A., 1986: An air–sea interaction theory for tropical cyclones. Part I: Steady-state maintenance. *J. Atmos. Sci.,* **43,** 585–604.

——, 1995: Sensitivity of tropical cyclones to surface exchange coefficients and a revised steady-state model incorporating eye dynamics. *J. Atmos. Sci.,* **52,** 3969–3976.

——, 2003: A similarity hypothesis for air–sea exchange at extreme wind speeds. *J. Atmos. Sci.,* **60,** 1420–1428.

——, K. C. DesAutels, C. Holloway, and R. Korty, 2004: Environmental control of tropical cyclone intensity. *J. Atmos. Sci.,* **61,** 843–858.

French, J. R., W. M. Drennan, J. A. Zhang, and P. G. Black, 2007: Turbulent fluxes in the hurricane boundary layer. Part I: Momentum flux. *J. Atmos. Sci.,* **64,** 1089–1102.

Gao, J., M. Xue, K. Brewster, and K. K. Droegemeier, 2004: A three-dimensional variational data analysis method with recursive filter for Doppler radars. *J. Atmos. Oceanic Technol.,* **21,** 457–469.

Gill, A., 1982: *Atmosphere–Ocean Dynamics.* Academic Press, 662 pp.

Haus, B. K., D. Jeong, M. A. Donelan, J. A. Zhang, and I. Savelyev, 2010: Relative rates of sea–air heat transfer and frictional drag in very high winds. *Geophys. Res. Lett.,* **37,** L07802, doi:10.1029/2009GL042206.

Hawkins, H. F., and D. T. Rubsam, 1968: Hurricane Hilda 1964. II. Structure and budgets of the hurricane on October 1, 1964. *Mon. Wea. Rev.,* **96,** 617–636.

——, and S. M. Imbembo, 1976: The structure of a small intense Hurricane Inez 1966. *Mon. Wea. Rev.,* **104,** 418–442.

Jarosz, E., D. A. Mitchell, D. W. Wang, and W. J. Teague, 2007: Bottom-up determination of air–sea momentum exchange under a major tropical cyclone. *Science,* **315,** 1707–1709.

Jeong, D., B. K. Haus, and M. E. Donelan, 2012: Enthalpy transfer across the air–water interface in high winds including spray. *J. Atmos. Sci.,* 2733–2748.

Jordan, C. L., 1958: Mean soundings for the West Indies area. *J. Meteor.,* **15,** 91–97.

Keeler, R. J., and S. M. Ellis, 2000: Observational error covariance matrices for radar data assimilation. *Phys. Chem. Earth,* **25,** 1277–1280.

Large, W. G., and S. Pond, 1981: Open ocean momentum flux measurements in moderate to strong winds. *J. Phys. Oceanogr.,* **11,** 324–336.

Lindzen, R., 1990: *Dynamics in Atmospheric Physics.* Cambridge University Press, 310 pp.

Machenhauer, B., 1979: The spectral method. *Numerical Methods Used in Atmospheric Models,* Vol. 2, A. Kasahara, Ed., GARP Publications Series 17, WMO/ICSU, 121–275.

Malkus, J. S., and H. Riehl, 1960: On the dynamics and energy transformations in steady-state hurricanes. *Tellus,* **12,** 1–20.

Marks, F. D., Jr., R. A. Houze Jr., and J. Gamache, 1992: Dual-aircraft investigation of the inner core of Hurricane Norbert. Part I: Kinematic structure. *J. Atmos. Sci.,* **49,** 919–942.

Miller, B. I., 1962: On the momentum and energy balance of Hurricane Helene (1958). National Hurricane Research Project Rep. 53, U.S. Weather Bureau, 19 pp.

——, 1964: A study of the filling of Hurricane Donna 1960: Over land. *Mon. Wea. Rev.,* **92,** 389–406.

Mohr, C. G., L. J. Miller, R. L. Vaughn, and H. W. Frank, 1986: The merger of mesoscale datasets into a common Cartesian format for efficient and systematic analysis. *J. Atmos. Oceanic Technol.,* **3,** 143–161.

Montgomery, M. T., M. M. Bell, S. D. Aberson, and M. L. Black, 2006: Hurricane Isabel (2003): New insights into the physics of intense storms. Part I: Mean vortex structure and maximum intensity estimates. *Bull. Amer. Meteor. Soc.,* **87,** 1335–1347.

——, R. Smith, and N. Van Sang, 2010: Sensitivity of tropical cyclone models to the surface drag coefficient. *Quart. J. Roy. Meteor. Soc.,* **136,** 1945–1953.

Nelder, J. A., and R. Mead, 1965: A simplex method for function minimization. *Comput. J.,* **7,** 308–313.

Ooyama, K. V., 1969: Numerical simulation of the life cycle of tropical cyclones. *J. Atmos. Sci.,* **26,** 3–40.

——, 1987: Scale controlled objective analysis. *Mon. Wea. Rev.,* **115,** 2479–2506.

——, 2002: The cubic-spline transform method: Basic definitions and tests in a 1D single domain. *Mon. Wea. Rev.,* **130,** 2392–2415.

Oye, R., C. Mueller, and S. Smith, 1995: Software for radar translation, visualization, editing, and interpolation. Preprints, *27th Conf. on Radar Meteorology,* Vail, CO, Amer. Meteor. Soc., 359–361.

Palmén, E., and H. Riehl, 1957: Budget of angular momentum and energy in tropical cyclones. *J. Meteor.,* **14,** 150–159.

Polak, E., 1971: *Computational Methods in Optimization.* Academic Press, 331 pp.

Powell, M. D., P. J. Vickery, and T. A. Reinhold, 2003: Reduced drag coefficient for high wind speeds in tropical cyclones. *Nature,* **422,** 279–283.

Press, W. H., S. A. Teukolsky, W. T. Vetterling, and B. P. Flannery, 2002: *Numerical Recipes in C++: The Art of Scientific Computing.* 2nd ed. Cambridge University Press, 1002 pp.

Purser, R. J., W.-S. Wu, D. Parrish, and N. M. Roberts, 2003: Numerical aspects of the application of recursive filters to variational statistical analysis. Part I: Spatially homogeneous and isotropic Gaussian covariances. *Mon. Wea. Rev.,* **131,** 1524–1535.

Rappaport, E. N., and Coauthors, 2009: Advances and challenges at the National Hurricane Center. *Wea. Forecasting,* **24,** 395–419.

Rosenthal, S. L., 1971: The response of a tropical cyclone model to variations in boundary layer parameters, initial conditions, lateral boundary conditions, and domain size. *Mon. Wea. Rev.,* **99,** 767–777.

Rotunno, R., and K. A. Emanuel, 1987: An air–sea interaction theory for tropical cyclones. Part II: Evolutionary study using a nonhydrostatic axisymmetric model. *J. Atmos. Sci.,* **44,** 542–561.

Shay, L. K., and S. D. Jacob, 2006: Relationship between oceanic energy fluxes and surface winds during tropical cyclone passage. *Atmosphere–Ocean Interactions,* Vol. II, W. Perrie, Ed., WIT Press, 115–137.

Smith, R. K., 2006: Accurate determination of a balanced axisymmetric vortex in a compressible atmosphere. *Tellus,* **58A,** 98–103.

——, and M. T. Montgomery, 2009: Hurricane boundary-layer theory. *Quart. J. Roy. Meteor. Soc.,* **36,** 1665–1670.

——, ——, and S. Vogl, 2008: A critique of Emanuel's hurricane model and potential intensity theory. *Quart. J. Roy. Meteor. Soc.,* **134,** 551–561.

Testud, J., P. H. Hildebrand, and W.-C. Lee, 1995: A procedure to correct airborne Doppler radar data for navigation errors using the echo returned from the earth's surface. *J. Atmos. Oceanic Technol.,* **12,** 800–820.

Vickery, P. J., D. Wadhera, M. D. Powell, and Y. Chen, 2009: A hurricane boundary layer and wind field model for use in engineering applications. *J. Appl. Meteor. Climatol.,* **48,** 381–405.

Willoughby, H. E., and M. B. Chelmow, 1982: Objective determination of hurricane tracks from aircraft observations. *Mon. Wea. Rev.,* **110,** 1298–1305.

Zhang, J. A., P. G. Black, J. R. French, and W. M. Drennan, 2008: First direct measurements of enthalpy flux in the hurricane boundary layer: The CBLAST results. *Geophys. Res. Lett.,* **35,** L14813, doi:10.1029/2008GL034374.

——, W. M. Drennan, P. G. Black, and J. R. French, 2009: Turbulence structure of the hurricane boundary layer between the outer rainbands. *J. Atmos. Sci.,* **66,** 2455–2467.

——, R. F. Rogers, D. S. Nolan, and F. D. Marks, 2011: On the characteristic height scales of the hurricane boundary layer. *Mon. Wea. Rev.,* **139,** 2523–2535.